



Enhanced Southern Ocean CO₂ outgassing as a result of stronger and poleward shifted southern hemispheric westerlies

Laurie C. Menviel^{1,2}, Paul Spence^{2,3}, Andrew E. Kiss^{4,5}, Matthew A. Chamberlain^{3,6}, Hakase Hayashida^{3,7}, Matthew H. England^{2,8}, and Darryn Waugh^{9,10}

¹Climate Change Research Centre, University of New South Wales, Sydney, NSW 2052, Australia

²The Australian Centre for Excellence in Antarctic Science, University of New South Wales, Sydney, NSW 2052, Australia

³Institute for Marine and Antarctic Studies and Australian Antarctic Program Partnership, University of Tasmania, Hobart, Australia

⁴Research School of Earth Sciences, Australian National University, Canberra, Australia

⁵Australian Research Council Centre of Excellence for Climate Extremes, Canberra, Australia

⁶CSIRO Oceans and Atmosphere, Hobart, Australia

⁷Application Laboratory, Japan Agency for Marine-Earth Science and Technology, Yokohama, Japan

⁸Centre for Marine Science and Innovation (CMSI), University of New South Wales, Sydney, NSW 2052, Australia

⁹School of Mathematics and Statistics, University of New South Wales, Sydney, NSW 2052, Australia

¹⁰Department of Earth and Planetary Sciences, John Hopkins University, Baltimore, USA

Correspondence: Laurie C. Menviel (l.menviel@unsw.edu.au)

Received: 3 March 2023 – Discussion started: 7 March 2023

Revised: 12 September 2023 – Accepted: 28 September 2023 – Published: 6 November 2023

Abstract. While the Southern Ocean (SO) provides the largest oceanic sink of carbon, some observational studies have suggested that the SO total CO₂ (tCO₂) uptake exhibited large (~ 0.3 GtC yr⁻¹) decadal-scale variability over the last 30 years, with a similar SO tCO₂ uptake in 2016 as in the early 1990s. Here, using an eddy-rich ocean, sea-ice, carbon cycle model, with a nominal resolution of 0.1°, we explore the changes in total, natural and anthropogenic SO CO₂ fluxes over the period 1980–2021 and the processes leading to the CO₂ flux variability. The simulated tCO₂ flux exhibits decadal-scale variability with an amplitude of ~ 0.1 GtC yr⁻¹ globally in phase with observations. Notably, two stagnations in tCO₂ uptake are simulated: between 1982 and 2000, and between 2003 and 2011, while re-invigorations are simulated between 2000 and 2003, as well as since 2012. This decadal-scale variability is primarily due to changes in natural CO₂ (nCO₂) fluxes south of the polar front associated with variability in the Southern Annular Mode (SAM). Positive phases of the SAM, i.e. stronger and poleward shifted southern hemispheric (SH) westerlies, lead to enhanced SO nCO₂ outgassing due to higher surface natural dissolved inorganic carbon (DIC) brought about by

a combination of Ekman-driven vertical advection and DIC diffusion at the base of the mixed layer. The pattern of the CO₂ flux anomalies indicate a dominant control of the interaction between the mean flow south of the polar front and the main topographic features. While positive phases of the SAM also lead to enhanced anthropogenic CO₂ (aCO₂) uptake south of the polar front, the amplitude of the changes in aCO₂ fluxes is only 25 % of the changes in nCO₂ fluxes. Due to the larger nCO₂ outgassing compared to aCO₂ uptake as the SH westerlies strengthen and shift poleward, the SO tCO₂ uptake capability thus reduced since 1980 in response to the shift towards positive phases of the SAM. Our results indicate that, even in an eddy-rich ocean model, a strengthening and/or poleward shift of the SH westerlies enhance CO₂ outgassing. The projected poleward strengthening of the SH westerlies over the coming century will, thus, reduce the capability of the SO to mitigate the increase in atmospheric CO₂.

1 Introduction

As a result of anthropogenic emissions of greenhouse gases, atmospheric CO₂ concentration (CO_{2atm}) increased from a natural level of 277 ppm in 1750 (Joos and Spahni, 2008) to 415 ppm in 2021 (Friedlingstein et al., 2022). The terrestrial biosphere and the ocean have, however, strongly mitigated the anthropogenic emissions of carbon, respectively absorbing ~ 31 and 24 % of the emissions (Le Quéré et al., 2018). The largest oceanic carbon sink is the Southern Ocean (SO), which has contributed ~ 40 % of the global oceanic CO₂ uptake in the 1990s (Sabine et al., 2004; Mikaloff-Fletcher et al., 2006). In the context of continued anthropogenic emissions of greenhouse gases, it is crucial to better understand the impact of climate change on atmosphere–ocean total (sum of anthropogenic and natural) CO₂ (tCO₂) fluxes.

There is evidence for large decadal variability in the total SO carbon uptake (LeQuéré et al., 2007; Matear and Lenton, 2008; Landschützer et al., 2015; Bushinsky et al., 2019; Gruber et al., 2019; Keppeler and Landschützer, 2019; Gruber et al., 2023). Observational estimates, covering the period 1982–2011, suggest that the total carbon uptake in SO was lower than expected in the 1990s but increased significantly between 2002 and 2011 to reach a maximum of 1.2 GtC yr⁻¹ in 2011 (LeQuéré et al., 2007; Landschützer et al., 2015; Gruber et al., 2019). Between 2011 and 2016, observational estimates combining the Surface Ocean CO₂ Atlas (SOCAT) and Southern Ocean Carbon and Climate Observations and Modeling (SOCCOM) suggest that the SO tCO₂ uptake weakened by ~ 0.4 GtC yr⁻¹ (Bushinsky et al., 2019; Gruber et al., 2019; Keppeler and Landschützer, 2019), while observational estimates only including SOCAT suggest the tCO₂ uptake stabilized between 2011 and 2016 and increased since 2017 (Landschützer et al., 2020). There is significant uncertainty associated with these estimates due to the sparsity of the data, particularly in the 1990s (Ritter et al., 2017; Gregor et al., 2018), and little information prior to 1982. In addition, this data scarcity might lead to a 39 % overestimation of the amplitude of SO decadal tCO₂ uptake variability (Gloege et al., 2021).

The SO circulation is mostly driven by SH westerly winds, which generate an equatorward Ekman transport and an associated upwelling of carbon-rich deep waters. Changes in the position and strength of the SH westerlies are linked to the dominant mode of atmospheric variability in the southern hemisphere, the SAM. Positive SAM phases, which are associated with poleward contraction and stronger than average westerly winds, have been observed between 1979 and 2000, particularly during austral summer and autumn (Thompson and Solomon, 2002; Fogt and Marshall, 2020). This intensification and poleward shift of the SH westerlies result from stratospheric ozone depletion and an increase in greenhouse gases (Arblaster and Meehl, 2006). However, due to stratospheric ozone recovery, a pause in the poleward intensifica-

tion of the SH westerlies has been observed between 2000 and ~ 2010 (Banerjee et al., 2020). The SAM trend is, however, positive since ~ 2010. The continued increase in greenhouse gases is taking over the ozone impact and is suggested to result in a long-term positive SAM trend over the 21st century (Thompson et al., 2011).

Numerical studies have highlighted the role of SH westerlies in modulating the upwelling of DIC-rich deep water and thus the carbon exchange between the atmosphere and the ocean. Stronger SH westerlies enhance the SO upwelling, leading to an oceanic loss of carbon and thus an increase in CO_{2atm} (Toggweiler, 1999; Lauderdale et al., 2013; Lovenduski et al., 2007, 2008; Munday et al., 2014; Lauderdale et al., 2017; Menviel et al., 2018). Changes in the strength and position of the SH westerlies associated with the SAM could, thus, significantly modulate interannual SO CO₂ fluxes (Resplandy et al., 2015). The increase in surface DIC as a result of stronger SO upwelling could, however, be partly mitigated by enhanced export production at the surface of the SO (Menviel et al., 2008; Hauck et al., 2013). In addition, the impact of latitudinal changes in the position of the SH westerlies on oceanic carbon and CO_{2atm} is uncertain, as it might depend on the initial position of the SH westerlies and on how the latitudinal changes in the SH westerlies impact the oceanic circulation (Völker and Köhler, 2013; Lauderdale et al., 2013, 2017).

Most of the numerical studies analysing the impact of SH westerly changes mentioned above focused on natural carbon. Given the increase in anthropogenic carbon emissions since 1870, the natural carbon cycle has been perturbed, and the impact of changes in the strength and position of the SH westerly winds on anthropogenic carbon uptake also needs to be taken into account. Only a few studies performed with coarse-resolution ocean models (Lovenduski et al., 2007, 2008) have assessed the impact of the SAM on total, anthropogenic and natural CO₂ fluxes. They found that positive phases of the SAM led to an outgassing of natural CO₂ (nCO₂), while enhancing the uptake of aCO₂, with the net effect being a reduction in the tCO₂ uptake. Lenton and Matear (2007) also simulated a reduction in tCO₂ uptake in response to the SAM but did not distinguish between the natural and anthropogenic contributions.

Some studies have thus attributed the weaker SO carbon uptake observed in the 1990s to a positive trend in the SAM (Marshall, 2003; LeQuéré et al., 2007; Lenton and Matear, 2007; Lovenduski et al., 2007, 2008; Gruber et al., 2023). This is supported by recent observations-based studies, which concluded that the multi-decadal surface SO *p*CO₂ variability, particularly the winter trend, was driven by the SAM (Gregor et al., 2018; Nevison et al., 2020), even though it was also suggested that on top of this multi-decadal trend net primary production could affect interannual variability (Gregor et al., 2018). On the other hand, McKinley et al. (2020) suggested that the lower 1990s CO₂ uptake was a response to the slower CO_{2atm} growth rate.

Regarding, the re-invigoration of the SO carbon uptake in the 2000s, Landschützer et al. (2015) suggested that it could not be attributed to the SAM because the ERA-interim reanalysis did not display the associated wind changes. Instead, they attributed the enhanced carbon uptake to increased solubility in the Pacific sector of the SO due to surface cooling and a weaker upwelling of DIC-rich waters in the Atlantic and Indian sectors of the SO. More recently, by analysing changes in SO $t\text{CO}_2$ fluxes between 1980 and 2016, Keppler and Landschützer (2019) suggested that the net effect of the SAM on $t\text{CO}_2$ uptake was nil and that, instead, the variability was arising from regional shifts in SO surface air pressure linked to zonal wavenumber 3.

There are, thus, uncertainties not only in the magnitude of the decadal variability but also in the processes controlling SO carbon uptake, and there is a need for further studies examining these issues. In addition, the impacts of mesoscale eddy activity on the SO oceanic circulation and transport of nutrient and carbon needs to be better constrained. The prevalent mesoscale eddy activity in the SO significantly influences heat, salt and nutrient transport, as well as the SO lateral and meridional overturning circulations. Mesoscale eddy transports generally act in the opposite sense to the wind-driven transport in the SO, and thus the response of the ocean circulation to changes in the winds varies across model studies. For example, a doubling of the magnitude of SH westerly winds doubles the simulated circumpolar transport in coarse-resolution models that poorly parameterize eddies, but this doubling does not occur in eddy-resolving simulations (Hallberg and Gnanadesikan, 2006; Farneti et al., 2010; Spence et al., 2010; Dufour et al., 2012; Morrison and Hogg, 2013; Munday et al., 2013). Further, Dufour et al. (2013) showed in an eddy-permitting ($\sim 0.5^\circ$ resolution) model that even though a strengthening and poleward shift of the SH westerlies, representing positive phases of the SAM, leads to stronger Ekman-induced northward natural DIC transport; a third of this is compensated by enhanced southward natural DIC transport through eddies. Dufour et al. (2013) also suggested that the higher surface DIC during positive phases of the SAM resulted from enhanced vertical diffusion at the base of the mixed layer and not from vertical advection.

Here, we analyse a simulation of the period 1980–2021 performed with an eddy-rich ocean, sea ice, biogeochemical model and forced with the 55-year Japanese Reanalysis for driving oceans (JRA55-do) (Tsujino et al., 2018) atmospheric fields to better understand the interannual to multi-decadal variability in SO natural, anthropogenic and total CO_2 fluxes and their links to changes in the SAM.

2 Methods

2.1 Models

Changes in SO carbon uptake are examined using a simulation performed with the eddy-rich ACCESS-OM2-01 global model configuration run under interannual forcing between 1958 and 2021. The ocean model is the Modular Ocean Model (MOM) version 5.1 (Griffies, 2012) with a nominal resolution of 0.1° and 75 vertical levels increasing smoothly in thickness from 1.1 m at the surface to 198.4 m at the bottom (5808.7 m depth). The ocean model is coupled to the thermodynamic-dynamic Los Alamos sea-ice model (CICE) version 5.1.2 (Hunke et al., 2017). ACCESS-OM2 is described in detail in Kiss et al. (2020), but the version presented here has many improvements as described in Solodoch et al. (2022). The main improvements are that the wind stress calculation now uses relative velocity over both ocean and sea ice (not just ocean), and the albedo of the ocean is now latitude-dependent following Large and Yeager (2009).

The ocean biogeochemical model is the Nutrient-Phytoplankton-Zooplankton-Detritus (NPZD) model WOMBAT (Whole Ocean Model of Biogeochemistry And Trophic-dynamics) (Kidston et al., 2011; Oke et al., 2013; Law et al., 2017). WOMBAT includes DIC, CaCO_3 , alkalinity, oxygen, phosphate and iron, that are linked to the phosphate uptake and remineralization through a constant Redfield ratio. The biogeochemical parameters are identical to those of the ACCESS-ESM1.5 model (Ziehn et al., 2020), apart from the pre-industrial $\text{CO}_{2\text{atm}}$ value. Two DIC tracers are included, a natural DIC (nDIC) and a total DIC (tDIC), with the difference between the two providing an estimate of anthropogenic DIC (aDIC). nDIC exchanges carbon with a constant pre-industrial $\text{CO}_{2\text{atm}}$ concentration of 284.32 ppm, whereas tDIC exchanges carbon with the time evolving, observed $\text{CO}_{2\text{atm}}$, which includes the current increase due to anthropogenic emissions. For the tDIC tracer, the $\text{CO}_{2\text{atm}}$ concentration is spatially uniform and annually averaged and follows the Ocean Model Intercomparison Project (OMIP) protocol until 2014 (Orr et al., 2017) and NOAA GML data thereafter, rising from 315.34 ppm in 1958 to 339.7 ppm in 1980 and 414.72 ppm in 2021 (Fig. 2a). The air–sea CO_2 exchange is a function of the difference in partial pressure of CO_2 at the air–sea interface, the wind speed (Wanninkhof, 1992) and sea ice concentration. This version also includes a two-way coupling of the ocean biogeochemistry with nutrient and algae carried in the sea ice model (Hayashida et al., 2021). Note that physical and biogeochemical changes in ocean simulations do not impact the atmospheric state, and in all simulations the longwave radiative forcing is given by the evolving JRA55-do fields over 1970–2021. Biogeochemical tracers also have no effect on the ocean or sea ice physical state (including shortwave penetration depth), and oxygen has no effect on other biogeochemical tracers.

2.2 Simulations

The model is forced by atmospheric conditions taken from the 55-year Japanese Reanalysis for driving oceans (JRA55-do) version 1.4, 1.5.0 and 1.5.0.1 (Tsujino et al., 2018), that now covers the period 1958 to 2021. JRA55-do allows calculation of air–sea fluxes of momentum, heat and freshwater at a 3 hourly time interval and with a horizontal resolution of 0.5625° . The model is forced by four 61-year cycles of JRA55-do v1.4 for the period 1958–2018. In cycle 1, the ocean model was initialized with modern-day temperature and salinity distributions derived from the World Ocean Atlas 2013 version 2 (Locarnini et al., 2013). Subsequent cycles used the final state of the previous cycle as the initial condition and proceeded through another JRA55-do v1.4 1958–2018 forcing cycle. Cycles 1–3 do not include biogeochemistry.

Here, we analyse cycle 4, which includes WOMBAT BGC and was extended from 2019 until the end of 2021 using JRA55-do v1.5.0 for 2019 and JRA55-do v1.5.0.1 thereafter. Ocean and ice physical fields were initialized from the values at the end of cycle 3. Biogeochemical fields other than oxygen were initialized at the start of cycle 4 (1958). A uniform 0.01 mmol m^{-3} initial value was used for phytoplankton, zooplankton, detritus and CaCO_3 . Initial alkalinity, tDIC and nDIC were interpolated from a 305 yr long spin-up run at 1° resolution (i.e. the first five cycles of OMIP2) (Mackallah et al., 2022). GLODAPv2 (Olsen et al., 2016) was used to initialize phosphate, and iron was initialized from the FEMIP median value (Tagliabue et al., 2016). Oxygen was initialized from GLODAPv2 at 1 January 1979 due to a configuration mistake; this has no effect on other variables. Initial phosphate and algae in the bottom 3 cm of sea ice were set to zero but quickly equilibrate with those in the surface ocean layer. The physical state of the ACCESS-OM2-01 global model is consistently simulated across all four, 61-year forcing cycles. Here, we skip the first 22 years of the fourth cycle (i.e. 1958–1980) from our analysis to allow the simulation to recover from the reset at the end of the previous cycle and focus our analysis on the period 1980–2021, following phase II of the Coordinated Ocean-ice Reference Experiments (CORE).

To better assess the impact of high model resolution, we also provide a comparison with the results of a 1° resolution configuration of ACCESS-OM2. This is based on that described by Kiss et al. (2020) but is forced with the newer JRA55-do v1.4 1958–2018 dataset and includes WOMBAT biogeochemistry. Specifically, this simulation corresponds to the final (sixth) cycle of omip2-spinup (Mackallah et al., 2022) after 33 cycles were performed as spin-up. Similar to ACCESS-OM2-01, in the version of ACCESS-OM2 used here the wind stress calculation uses relative velocity over both ocean and sea ice and the albedo of the ocean is latitude-dependent following Large and Yeager (2009). The 1° configuration has flow-dependent Gent and McWilliams

(1990) parameterization of unresolved mesoscale eddies, as described in Kiss et al. (2020).

2.3 Analysis

For consistency with the forcing, the SAM index is calculated from the JRA55-do dataset with the methodology described in Stewart et al. (2020). The SAM index as calculated from the JRA55-do dataset captures the SAM index based on observations (Marshall, 2003; Stewart et al., 2020) well.

In this study, the SO polar front (PF) and sub-Antarctic front (SAF) are defined as the 1.2°C annual minimum surface temperature contour and 4°C isotherm at 400 m depth, respectively, following the definition of Sokolov and Rintoul (2009). Their simulated zonal mean latitude locations are 56.3 and 48.2°S , respectively.

Oceanic natural $p\text{CO}_2$ is a function of nDIC, alkalinity (ALK) as well as ocean temperature (T) and salinity (Sal). Changes in $p\text{CO}_2$ can, thus, be described as:

$$\Delta p\text{CO}_2 = \frac{\partial(p\text{CO}_2)}{\partial(\text{DIC})} \cdot \Delta\text{DIC} + \frac{\partial(p\text{CO}_2)}{\partial(\text{ALK})} \cdot \Delta\text{ALK} + \frac{\partial(p\text{CO}_2)}{\partial(\text{Sal})} \cdot \Delta\text{Sal} + \frac{\partial(p\text{CO}_2)}{\partial(T)} \cdot \Delta T. \quad (1)$$

To better understand the processes leading to surface ocean $p\text{CO}_2$ changes, we can estimate the $p\text{CO}_2$ change from each of the above variables separately. Broecker et al. (1979) derived that if ALK, salinity and temperature are constant, then:

$$\frac{\partial \ln(p\text{CO}_2)}{\partial \ln(\text{DIC})} = \gamma_{\text{DIC}}, \quad (2)$$

with γ_{DIC} being the Revelle factor of DIC. Equation (1) can be re-written as:

$$\frac{\text{DIC}}{p\text{CO}_2} \cdot \frac{\partial p\text{CO}_2}{\partial \text{DIC}} = \gamma_{\text{DIC}}. \quad (3)$$

One can then derive the $p\text{CO}_2$ change due to a change in DIC ($\Delta p\text{CO}_{2\text{DIC}}$) as:

$$\Delta p\text{CO}_{2\text{DIC}} = \gamma_{\text{DIC}} p\text{CO}_2 \frac{\Delta \text{DIC}}{\text{DIC}}. \quad (4)$$

Here, we use a mean high latitude estimate for γ_{DIC} of 13.3 (Sarmiento and Gruber, 2006) to estimate $p\text{CO}_{2\text{DIC}}$. $p\text{CO}_2$ sensitivities to ALK and salinity can be derived with similar equations:

$$\Delta p\text{CO}_{2\text{ALK}} = \gamma_{\text{ALK}} p\text{CO}_2 \frac{\Delta \text{ALK}}{\text{ALK}}, \quad (5)$$

and

$$\Delta p\text{CO}_{2\text{Sal}} = \gamma_{\text{Sal}} p\text{CO}_2 \frac{\Delta \text{Sal}}{\text{Sal}}, \quad (6)$$

with $\gamma_{\text{ALK}} = -12.6$ and $\gamma_{\text{Sal}} = 1$ (Sarmiento and Gruber, 2006).

Finally, Takahashi et al. (1993) suggest that the $p\text{CO}_2$ sensitivity to temperature (T) follows the relationship:

$$\frac{\partial \ln(p\text{CO}_2)}{\partial T} = 0.0423 \text{ } ^\circ\text{C}^{-1}. \quad (7)$$

This implies (Takahashi et al., 2002, 2009) that the change in $p\text{CO}_2$ due to temperature is:

$$\Delta p\text{CO}_{2T} = (e^{0.0423\Delta T} - 1)p\text{CO}_2. \quad (8)$$

Changes in oceanic remineralized carbon concentration (C_{rem}) between 1980 and 2021 are estimated as follows:

$$\Delta C_{\text{rem}} = R_{C/P} \Delta \text{PO}_{4\text{rem}}, \quad (9)$$

with

$$\Delta \text{PO}_{4\text{rem}} = R_{P/O_2} \Delta \text{AOU}. \quad (10)$$

AOU is the apparent oxygen utilization and is the difference between the dissolved oxygen at saturation (as a function of temperature and salinity) and the simulated dissolved oxygen concentration. $R_{C/P}$ and R_{P/O_2} are the Redfield ratios equal to 106/1 and 1/172, respectively.

3 Results

3.1 Mean CO_2 flux patterns

Performance of the multi-resolution ACCESS-OM2 model suite is discussed in Kiss et al. (2020). The eddy-rich ACCESS-OM2-01 model at 0.1° resolution provides a reasonable and consistent representation of the state of the ocean, with a particularly good representation of the SO circulation structure, dense shelf water formation and abyssal overturning cell (Morrison et al., 2020). The simulated horizontal and vertical gradients in tDIC, alkalinity and dissolved oxygen (O_2) in the Southern Ocean are in good agreement with observations (Olsen et al., 2016) (Fig. S1). The absolute values of tDIC and alkalinity are $\sim 60 \mu\text{mol kg}^{-1}$ lower than those estimated by GLODAP. This bias might lead to a ~ 10 – 15 ppm underestimation of the total $p\text{CO}_2$ of SO waters, which does not seem to significantly impact the SO t CO_2 uptake, as detailed below. The concentrations of the different biogeochemical tracers are not constant through the simulation since the atmospheric forcing varies (among other reasons); however, the trends averaged over the Southern Ocean and at different depths are much lower than 1% (Fig. S2). In addition, apart from the nDIC at intermediate depth and dissolved O_2 at depth, the trends are similar in the 0.1 and 1° resolution, even though the 1° resolution has been equilibrated for a longer time. This indicates that both the 0.1 and 1° simulations can be used to study the SO biogeochemical response to the atmospheric forcing.

We first assess the performance of the model by comparing the time-mean simulated SO t CO_2 fluxes to observational

estimates (Fig. 1a, b). SOCAT version 6 (Bakker et al., 2016) provides surface ocean CO_2 measurements. However, due to the spatial and temporal heterogeneity of these measurements, it does not provide an appropriate dataset for a comparison with simulated fields. To fill this gap, Landschützer et al. (2016) developed a method to provide a global gridded monthly observational estimate. The ocean is first clustered into biogeochemical provinces using a self-organizing map (SOM). Then, within each biogeochemical province, $p\text{CO}_2$ estimates are generated based on a non-linear relationship between the SOCATv6 observations and the CO_2 driver variables through a feed-forward neural network (FFN) approach. If averaged over the available period of 1982–2021, the observationally derived SOM-FFN dataset (Landschützer et al., 2020) (Fig. 1a) displays a strong t CO_2 uptake north of 50° S ($-1.59 \text{ mol m}^{-2} \text{ yr}^{-1}$, zonal average between 50 and 35° S) and a weak t CO_2 uptake ($-0.38 \text{ mol m}^{-2} \text{ yr}^{-1}$) south of 50° S, even though there are some areas with outgassing ($\sim 0.2 \text{ mol m}^{-2} \text{ yr}^{-1}$) south of 50° S.

These features are relatively well reproduced by the simulated t CO_2 fluxes (Fig. 1b), which display a similar strong uptake ($-1.59 \text{ mol m}^{-2} \text{ yr}^{-1}$) north of 50° S, that is generally north of the SAF (Sokolov and Rintoul, 2009). As in the observations, some t CO_2 outgassing ($\sim 0.4 \text{ mol m}^{-2} \text{ yr}^{-1}$) is simulated south of the SAF, but particularly south of the PF. While both observational estimates and simulation suggest a t CO_2 outgassing south of the PF at 0–60° E, 150–180° E, and downstream of the Drake passage, the simulated t CO_2 outgassing is particularly confined to some hotspots, namely over the eastern part of the Southeast Indian Ridge, east of Drake Passage, and over the Southwest Indian Ridge (Fig. 1b). Overall, a similarly weak t CO_2 uptake ($-0.59 \text{ mol m}^{-2} \text{ yr}^{-1}$) is estimated south of 50° S.

These fluxes can be decomposed into their n CO_2 and a CO_2 components, thus highlighting an uptake of a CO_2 nearly everywhere south of 35° S (Fig. 1d), with two zonally averaged maximum a CO_2 uptakes at 42 and 55° S (Fig. S3f). While this is broadly consistent with observational estimates, the observations suggest a maximum a CO_2 uptake at 50° S (Gruber et al., 2023). By contrast, an outgassing of n CO_2 is simulated south of the PF and in the frontal zone of the Indian sector (Figs. 1c and S3e).

The upwelling of DIC-rich deep waters south of the PF (Figs. 1e and S3c) and the subsequent northward advection of these waters (Fig. S3b) contribute to the n CO_2 outgassing south of 50° S. Through Ekman transport, surface waters in the SO move equatorward (Fig. S3b), and nutrients and DIC are consumed by phytoplankton, leading to a maximum detritus flux at $\sim 42^\circ$ S (Fig. S3d) and n CO_2 ocean uptake north of the SAF (Fig. S3e), where Antarctic Intermediate Waters (AAIW) and Subantarctic Mode Waters (SAMW) are formed. Within the model framework, the detritus flux at 100 m depth provides an estimate of export production.

The pattern of mean simulated SO CO_2 fluxes are similar in the 0.1° (ACCESS-OM2-01) and 1° (ACCESS-OM2)

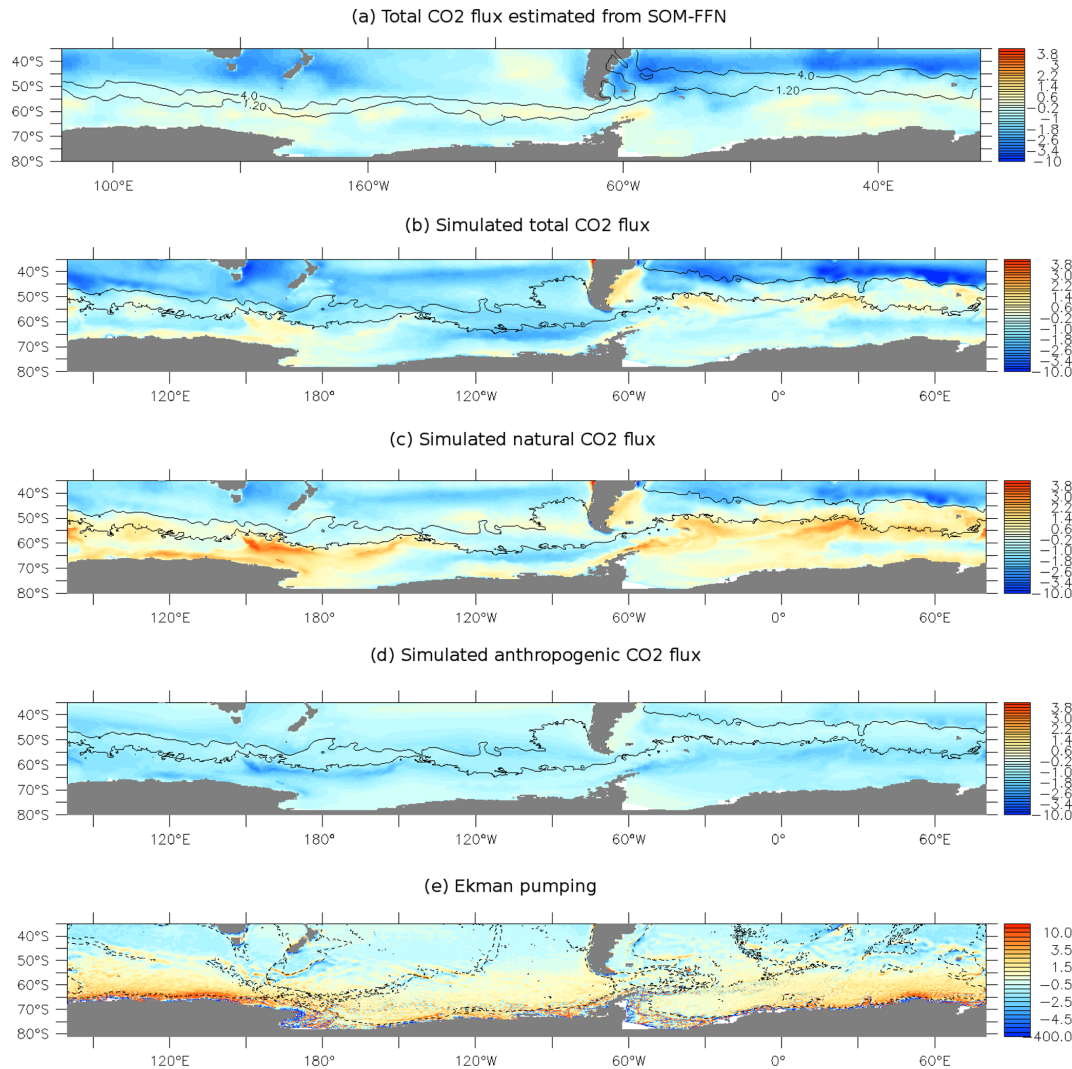


Figure 1. (a) Total ocean to atmosphere CO_2 flux ($\text{molC m}^{-2} \text{yr}^{-1}$) as estimated from the SOM-FFN for the period 1982–2021 (Landschützer et al., 2016, 2020). The black contours indicate (from south to north) the northern edges of the polar front (PF) and the sub-Antarctic front (SAF) using the definition of Sokolov and Rintoul (2009) and the temperature data from the World Ocean Atlas (Locarnini et al., 2013). Simulated (b) total, (c) natural and (d) anthropogenic ocean to atmosphere CO_2 flux ($\text{molC m}^{-2} \text{yr}^{-1}$) averaged over the period 1982–2021 in the 0.1° ACCESS-OM2-01. The black contours indicate the northern edges of the PF and SAF using the definition of Sokolov and Rintoul (2009). (e) Ekman pumping ($\times 10^{-6} \text{m s}^{-1}$) averaged over the period 1982–2021 in the numerical experiment. The black lines overlaid represent the 2500 m depth bathymetry contour.

version of the model (Figs. S3 and S4), implying a dominant effect of the large-scale oceanic circulation on the CO_2 fluxes. The main differences are that the tCO_2 , nCO_2 and aCO_2 flux hotspots over the eastern part of the Southeast Indian Ridge, east of the Drake Passage and over the Southwest Indian Ridge are more pronounced in the ACCESS-OM2-01 (Fig. 1b, c, d) than in the ACCESS-OM2 (Fig. S4b, c, d), implying a stronger interaction between circulation and topography in the eddy-rich model.

3.2 Temporal changes in CO_2 fluxes

We now look at the time evolution of SO CO_2 fluxes since 1980 (Fig. 2). From 1980–2021, the SO nCO_2 uptake (Fig. 2c, grey and shading) reduces by $\sim 0.28 \text{GtC yr}^{-1}$ (mean slope of 0.07GtC yr^{-1} per decade). The nCO_2 uptake is stronger than the 1980–2021 mean before the mid-1990s and weaker after that (Fig. 2c). On top of the long-term trend, the nCO_2 flux displays a large ($\sim 0.15 \text{GtC yr}^{-1}$) decadal-scale variability. nCO_2 fluxes are strongly correlated with the SAM index calculated from the JRA-55do dataset ($R = 0.62$ for annual mean data and $R = 0.84$ with a 5-year

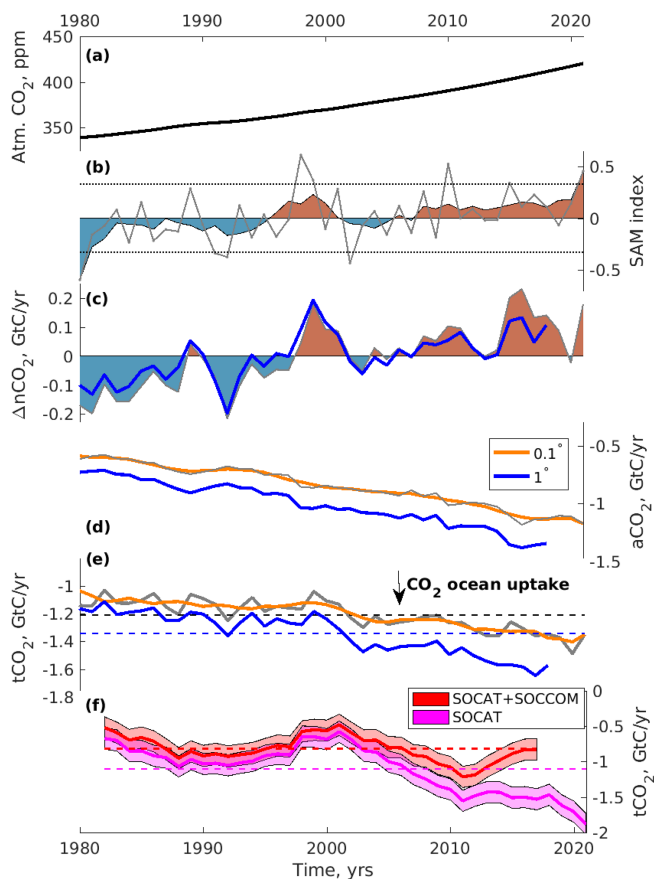


Figure 2. Time series of (a) annual mean atmospheric CO₂ concentration used as forcing, (b) SAM index calculated from the JRA55-do dataset (Stewart et al., 2020). The horizontal dotted lines represent the thresholds used to define positive and negative SAM in the composites. Simulated integrated ocean to atmosphere CO₂ fluxes in the ACCESS-OM2-01 (0.1°, annual mean in grey and 5 years running mean in orange) and ACCESS-OM2 (1°, annual mean in blue) simulations: (c) nCO₂, (d) aCO₂ and (e) tCO₂. (f) SO tCO₂ flux as derived from the SOM-FFN (red) including both the SOCAT and SOCCOM data (Bushinsky et al., 2019) and (magenta) only including the SOCAT data (Landschützer et al., 2020). The shading represents an uncertainty of 0.15 GtC yr⁻¹. All the CO₂ fluxes are integrated over the SO (35–80° S) and are in GtC yr⁻¹. Dashed horizontal lines represent the mean over 1980–2021 or over the available period.

smoothing, Fig. 2b), with periods of weak nCO₂ uptake associated with positive phases of the SAM. This SAM link is largely related to changes in the strength of the zonal SO wind stress (Fig. S5d, $R = 0.62$ for yearly data, 0.92 with 5-year smoothing), even though a poleward displacement of the maximum wind stress also reduces the nCO₂ uptake (Fig. S5g, $R = -0.4$).

Since the SAM index displays a trend towards the positive phase between 1980 and 2021, the correlation mentioned above includes both interannual variability, as well as decadal-scale changes. To also assess whether changes in

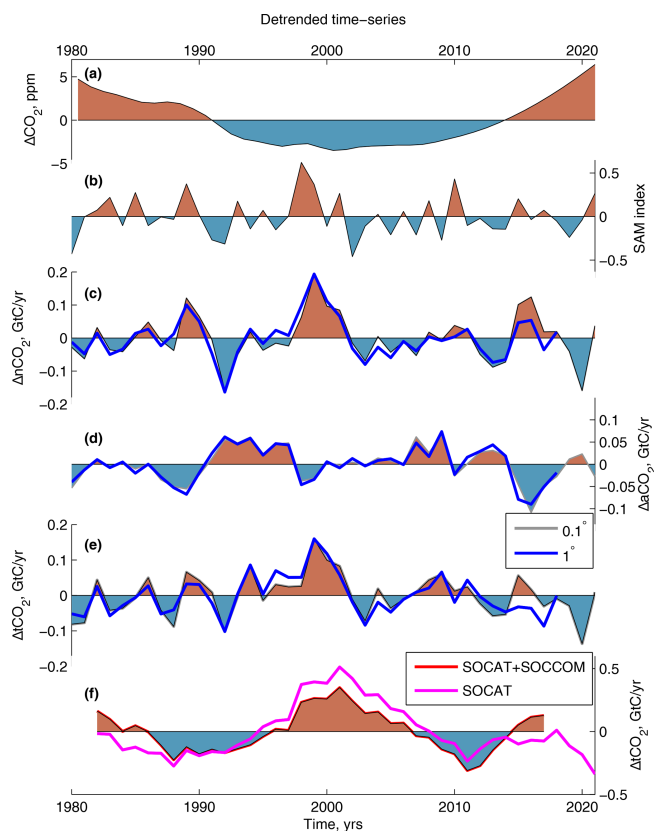


Figure 3. Detrended annual mean time series of (a) atmospheric CO₂ (ppm) used as forcing, (b) SAM index calculated from the JRA55-do dataset (Stewart et al., 2020). Detrended annual-mean simulated integrated ocean to atmosphere annual mean detrended CO₂ fluxes in the ACCESS-OM2-01 (0.1°, grey, with light blue and red shadings indicating positive and negative anomalies with respect to the mean) and the ACCESS-OM2 (1°, blue) simulations: (c) nCO₂, (d) aCO₂, (e) tCO₂. (f) Detrended SO tCO₂ flux as derived from the SOM-FFN including both the SOCAT and SOCCOM data (red) (Bushinsky et al., 2019) and including the SOCAT data only (magenta) (Landschützer et al., 2020). All the CO₂ fluxes are integrated over the SO (35–80° S) and are in GtC yr⁻¹.

the SAM significantly impact nCO₂ fluxes on an interannual timescale, we look into the detrended SAM and nCO₂ flux time-series (Fig. 3b and c). The correlation between the detrended SAM index and detrended nCO₂ flux is significant ($p \leq 0.05$) and equals 0.51 (Fig. S5a).

To assess the impact of high resolution, and thus the lack of parameterized eddies, on the simulated CO₂ fluxes, the results of the 1° version of ACCESS-OM2 are also included (Fig. 2c, blue). If zonally averaged, they closely track the results of ACCESS-OM2-01, displaying a similar trend and interannual variability in SO nCO₂ fluxes.

The simulated aCO₂ uptake increases by 0.56 GtC yr⁻¹ over the period 1980–2021 (Fig. 2d, grey and orange) noting that the CO₂atm, which is a forcing of the model, also increases during that time (Fig. 2a). To better highlight vari-

ability in the $a\text{CO}_2$ flux, we detrend it and plot the anomaly with respect to the 1980–2021 mean (Fig. 3d). The $a\text{CO}_2$ uptake also features decadal-scale variability, but with an amplitude that is about 30 % lower than for $n\text{CO}_2$. A weak but significant ($p \leq 0.05$) relationship between $a\text{CO}_2$ uptake and the detrended SAM index is simulated ($R = -0.42$, Fig. S5b). Increased $a\text{CO}_2$ uptake occurs when the westerlies strengthen ($R = -0.36$, Fig. S5e). While the 1° model displays a slightly larger $a\text{CO}_2$ uptake, the trends are similar between 1980 and 2018 (Fig. 2d, blue), and the detrended fluxes track each other very closely (Fig. 3d).

The combined effect of reduced $n\text{CO}_2$ uptake and increased $a\text{CO}_2$ uptake (mostly due to the increase in $\text{CO}_{2\text{atm}}$) lead to a 0.36 GtC yr^{-1} increase in $t\text{CO}_2$ uptake between 1980 and 2021 (Fig. 2e). The SO $t\text{CO}_2$ uptake in the 0.1 and 1° simulations track each other fairly closely, even though the trend is larger in the 1° ($-0.015 \text{ GtC yr}^{-2}$) than in the 0.1° ($-0.013 \text{ GtC yr}^{-2}$) (Fig. 2e, blue compared to grey). The simulated $t\text{CO}_2$ fluxes can be compared to the observational estimates derived from the SOM-FFN based on the SOCAT and SOCCOM biogeochemistry floats from 1982 to 2017 (red) (Landschützer et al., 2019; Bushinsky et al., 2019) and based on SOCAT only from 1982–2021 (magenta) (Landschützer et al., 2020) (Fig. 2g). The simulated $t\text{CO}_2$ flux and observational estimates of $t\text{CO}_2$ flux are well correlated ($R = 0.55$ for SOCAT and SOCCOM compared to ACCESS-OM2-01 and $R = 0.79$ for SOCAT only compared to ACCESS-OM2-01).

In the 0.1° experiment, the simulated $t\text{CO}_2$ uptake increases by only $0.003 \text{ GtC yr}^{-2}$ between 1980 and 1998 (Fig. 2e), in agreement with both observational estimates (Fig. 2f). While the simulated $t\text{CO}_2$ uptake decreases between 1998 and 2001 as in the observations, the magnitude of this simulated change is smaller than in the observational estimates. Similarly, while both simulation and observational estimates display an increase in $t\text{CO}_2$ uptake in the early 2000s, the reinvigoration only lasts until 2003 in the simulation, while it lasts until 2010 in both observational datasets. Finally, similar to the SOCAT only product, the simulation suggests a small re-invigoration of the $t\text{CO}_2$ uptake since 2012, while the SOCAT + SOCCOM product suggests a decrease in $t\text{CO}_2$ uptake. While the simulated $t\text{CO}_2$ changes are within the uncertainty range of the observational estimates ($\pm 0.15 \text{ GtC yr}^{-1}$) (Bushinsky et al., 2019) for most of the simulated period, the simulated variations are lower and outside of the uncertainty range between 1998 and 2005.

Since changes in $t\text{CO}_2$ flux are also impacted by the $\text{CO}_{2\text{atm}}$ increase, we detrend the SO $t\text{CO}_2$ flux and plot the anomaly with respect to the detrended 1980–2021 mean to properly assess the decadal-scale variability. The detrended $t\text{CO}_2$ fluxes (Fig. 3e) present variations similar to the detrended $n\text{CO}_2$ fluxes (Fig. 3c), with reduced total uptake during positive phases of the SAM (Fig. 3b). The $n\text{CO}_2$ flux variability dominates the changes in $t\text{CO}_2$ uptake with a strengthening of the winds and a poleward shift both reducing the

$t\text{CO}_2$ uptake (Figs. 3c, e and S5f, i). The detrended fluxes in the 0.1 and 1° simulations track each other very closely (Fig. 3e).

The correlation between detrended simulated and observationally estimated $t\text{CO}_2$ fluxes are 0.35 for SOCAT and SOCCOM (Bushinsky et al., 2019) and 0.37 for SOCAT only Landschützer et al. (2020). The two main disagreements are in the mid 1990s and the late 2000s and early 2010s, when the model simulates relatively low $t\text{CO}_2$ uptake (Fig. 3e), while the observational estimates suggest high $t\text{CO}_2$ uptake (Fig. 3f). During these two periods the detrended $n\text{CO}_2$ fluxes are small, whereas the detrended $a\text{CO}_2$ fluxes are positive. These periods of low $t\text{CO}_2$ uptake in the model are, thus, due to reduced $a\text{CO}_2$ uptake, probably resulting from the atmospheric CO_2 forcing.

3.3 Processes leading to changes in natural CO_2 fluxes

3.3.1 Multi-decadal trend

To better understand the processes driving the multi-decadal increase in SO $n\text{CO}_2$ outgassing, we look into the surface water natural $p\text{CO}_2$ trend and the contributions to this trend of changes in nDIC, ALK, surface temperature (SST) and salinity (SSS, Fig. 4) in ACCESS-OM2-01.

The largest positive natural $p\text{CO}_2$ trend is simulated south of the PF and particularly south of 60° S , in the area of high upward Ekman pumping (Fig. 1e). The natural $p\text{CO}_2$ trends are particularly large in the Atlantic and Indian sectors. This is due to an increase in surface nDIC (Fig. 4b), partly compensated by an increase in ALK (Fig. 4c). We also note an area displaying a negative natural $p\text{CO}_2$ trend, off the Ross Sea and extending eastward. This is due to a decrease in nDIC, partly compensated by a decrease in ALK. On the other hand, the changes in SST and SSS (Fig. 4d, e) are not contributing significantly to the multi-decadal changes in surface natural $p\text{CO}_2$.

Taking also into account that changes in detritus flux are concentrated north of 50° S (Fig. S3k), these results suggest that changes in oceanic circulation, and particularly the upwelling strength (Fig. S3j) and subsequent northward Ekman transport (Fig. S3i), are responsible for the positive $n\text{CO}_2$ outgassing trend (Figs. 2c and S3l). The non-thermal natural $p\text{CO}_2$ changes are, indeed, significantly correlated with changes in the strength of the westerlies in each sector of the Southern Ocean (Fig. S6a, d). The inter-basin differences in SH westerlies latitudinal trends probably contributed to the relatively larger increase in surface natural $p\text{CO}_2$ in the Atlantic and Indian sectors compared to the Pacific sector (Fig. S6e). Indeed, in the JRA55-do dataset there is a ~ 1.5 and $\sim 1^\circ$ poleward shift in the Atlantic and Indian sectors, respectively, starting in the late 1990s, while there are no significant latitudinal changes in the Pacific sector (Fig. S6e). This is broadly consistent with observations, which suggest a $\sim 1^\circ$ poleward shift in the Atlantic and Indian sector and a

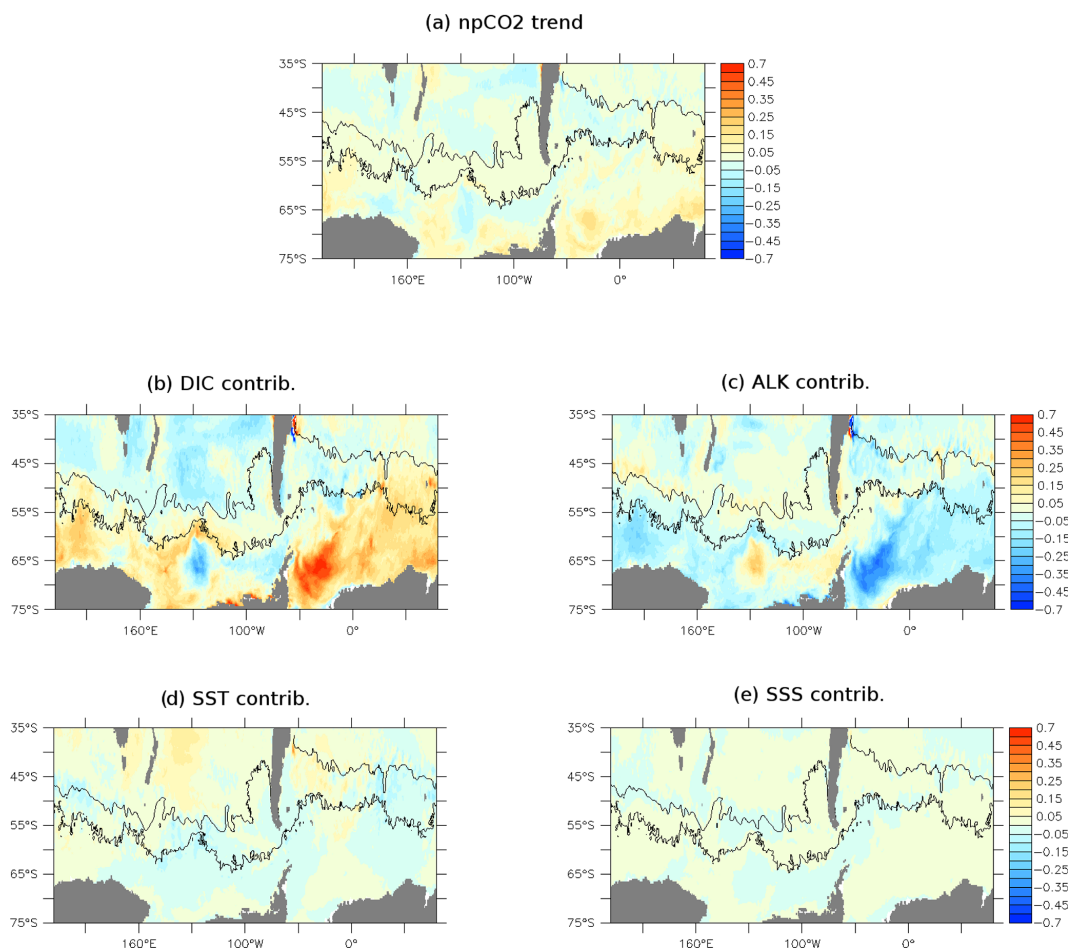


Figure 4. (a) Natural $p\text{CO}_2$ trend (ppm per decade) between 1981 and 2021 and (b) nDIC, (c) ALK, (d) SST and (e) SSS contributions to the natural $p\text{CO}_2$ trend (ppm per decade) for the ACCESS-OM2-01 simulation.

$\sim 1^\circ$ equatorward shift in the Pacific sector since the 1980s (Waugh et al., 2020).

The processes leading to the positive natural $p\text{CO}_2$ trend can be further assessed by analysing the changes in SO nDIC between 1980 and 2021 (Fig. 5). An increase in nDIC is simulated within the upwelling branches of the North Atlantic Deep Water, Indian Deep Water and Pacific Deep Water (Fig. 5a–c), while the nDIC concentration is reduced below 3000 m depth, particularly in the Atlantic and Indian sectors as well as within the SAMW. The nDIC increases within the upwelling branches are mostly due to an increase in remineralized DIC (Fig. 5d–f). It is unlikely that the detritus flux increase centred at 42° S (Fig. S3k) is responsible for these positive remineralized DIC anomalies; instead, they most likely indicate a higher proportion of older and deeper waters, consistent with enhanced SO upwelling.

The negative nDIC anomalies at depth are concentrated in the Antarctic Bottom Water (AABW) formation regions (Weddell Sea, Ross Sea and Adelie coast) and in the subsequent transport regions westward around Antarctica (Morrison et al., 2020; Solodoch et al., 2022). The negative

nDIC anomalies at depth and within the SAMW are due to reduced remineralized DIC content, most likely implying higher transport rates of SAMW and AABW.

A reduced vertical nDIC gradient is simulated in all basins south of the SAF, due to higher nDIC in the top ~ 1000 m depth and reduced nDIC at depth. This pattern is consistent with enhanced SO upwelling resulting from a strengthening and poleward shift of the SH westerlies since 1980.

We next look at the evolution of nDIC in the subsurface of the SO between 1980 and 2021 and assess its link to the surface variability (Fig. 6). The nDIC concentration at 1000 m depth gradually increases at all latitudes during that time period, but with a steepest increase between 45 and 60° S (Fig. 6b), which corresponds to the upwelling branch of the Indian Deep Water, Pacific Deep Water and North Atlantic Deep Water. At 400 m depth, nDIC also increases south of the SAF due to the enhanced upwelling of nDIC-rich deep waters (Fig. 6a). On the other hand, nDIC at 400 m depth decreases north of the SAF within SAMW. This contrasting behaviour north and south of the SAF could be linked to the poleward shift of the SH westerlies. At both 400 and 1000 m

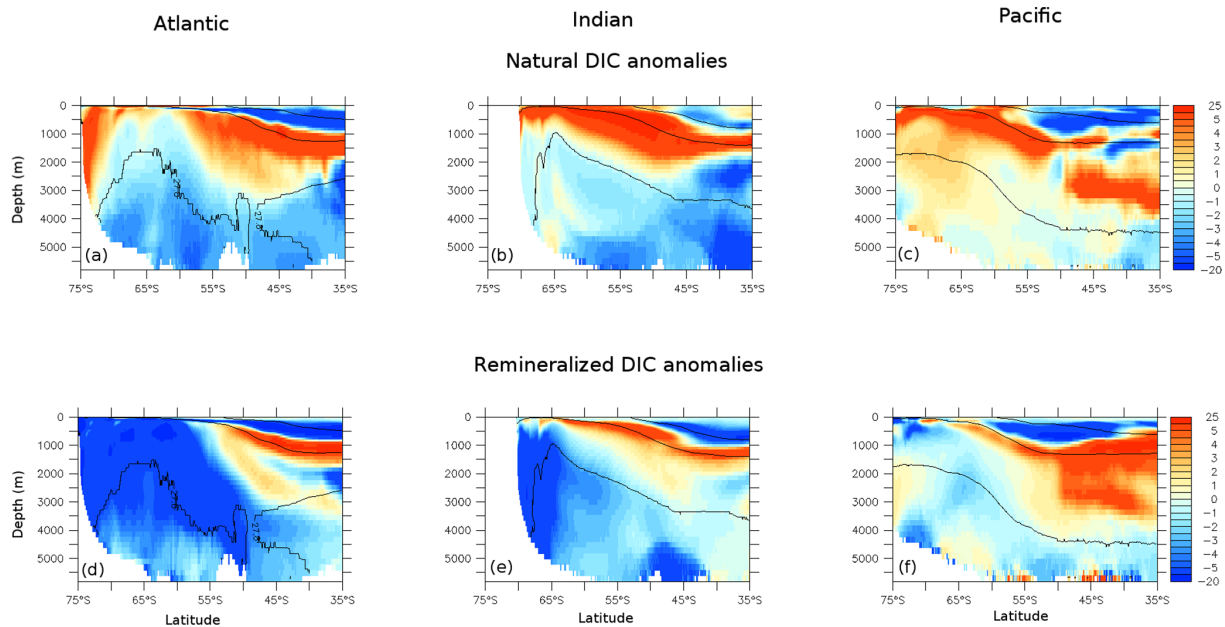


Figure 5. Zonally averaged (a–c) natural DIC and (d–f) remineralized DIC (C_{rem} , mmol m^{-3}) averaged over (a, d) the Atlantic, (b, e) the Indian and (c, f) the Pacific for years 2017–2021 compared to 1980–1982 for the ACCESS-OM2-01 simulation. The density of the AABW ($\geq 1028.31 \text{ kg m}^{-3}$), the AAIW ($1027.5 \geq \text{AAIW} \geq 1026.95 \text{ kg m}^{-3}$) and the SAMW ($\leq 1026.95 \text{ kg m}^{-3}$) are overlaid.

depth, decadal-scale DIC variations are visible (Fig. 6). The fast response of subsurface DIC to the surface forcing is consistent with nDIC changes being due to Ekman pumping and associated isopycnal displacement, which respond quickly to surface forcing (Waugh and Haïne, 2020).

3.3.2 Impact of the SAM on SO CO₂ fluxes

Overall, an increase in natural CO₂ outgassing is simulated in SO (Fig. 2c) as a response to an increase in surface nDIC. Superimposed on this trend are increases in nCO₂ outgassing during positive phases of the SAM (Figs. 2b, c and 3b, c). To better highlight the quantitative impact of positive phases of the SAM, we perform a composite of the years in which the annual mean SAM index as calculated from the JRA55-do dataset was greater than 0.33 (i.e. 1998, 1999, 2010, 2015 and 2021) and compare this to a composite of negative SAM years (SAM index ≤ -0.33 : 1980, 1991, 1992, 2002).

During these strong positive phases of the SAM, a significant increase ($\geq 1 \text{ mol m}^{-2} \text{ yr}^{-1}$) in nCO₂ outgassing is simulated south of the PF (Fig. 7a). Some enhanced nCO₂ outgassing is also simulated between the SAF and PF in the Indian and southwest Pacific sector, as well as north of the SAF in the Pacific sector. This nCO₂ outgassing mostly results from an increase in surface nDIC concentration (Figs. 7b and 9b).

The stronger and poleward shifted westerlies during positive phases of the SAM enhance the Ekman-driven vertical DIC advection south of the PF (Figs. 7g and 8b). The associated deepening of the mixed layer also drives an increase in

vertical DIC diffusion at the base of the mixed layer (Figs. 7e, f and 8c). South of the PF, the Ekman-driven vertical DIC advection and vertical diffusion at the base of the mixed layer contribute equally to the DIC increase (2.8 GtC yr^{-1} , Fig. 8b, c). The eddy-driven vertical DIC advection (taken as the difference between the vertical DIC advection and the Ekman-driven vertical DIC advection) further contributes to the higher surface DIC south of 60° S ($+0.7 \text{ GtC yr}^{-1}$, not shown). However, north of the PF, the Ekman-driven vertical DIC advection decreases surface DIC, while vertical diffusion at the base of the mixed layer leads to a DIC increase in the mixed layer. In this simulation, changes in biological export of carbon are two orders of magnitude smaller than the Ekman-driven and vertical diffusion contributions and, therefore, do not significantly affect changes in nCO₂ fluxes (Fig. 8d).

Due to the long-term shift towards positive phases of the SAM, the composite of positive SAM is shifted towards more recent years than the composite of negative phases. If we correct for this (i.e. assuming that the aCO₂ uptake follows a linear trend), then an anomalous aCO₂ uptake is simulated south of the PF (Fig. 7c), in regions where a stronger nCO₂ outgassing is simulated (Fig. 7a). The amplitude of the aCO₂ anomalies are, however, only equivalent to $\sim 25\%$ of the nCO₂ anomalies (Figs. 7a, c and 8e, f black line). As a result, reduced tCO₂ uptake is simulated south of the PF during positive phases of the SAM (Fig. S7b). If a similar correction is applied to compensate for the difference in mean year between the positive and negative SAM composites, then an

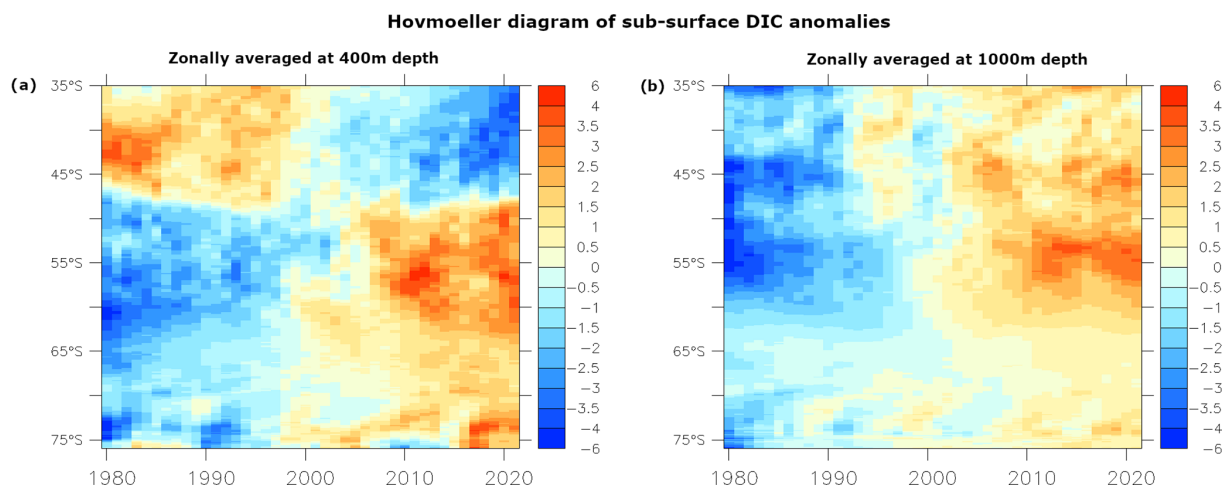


Figure 6. Hovmöller diagram over the period 1980–2021 of zonally averaged nDIC anomalies (mmol m^{-3}) as a function of time and latitude at (a) 400 and (b) 1000 m depth compared to the time average nDIC in the ACCESS-OM2-01 simulation.

anomalous tCO_2 outgassing is simulated almost everywhere in the SO (Figs. 7d and 8g, black line).

It is interesting to note that south of the PF, the regions of maximum nCO_2 outgassing and aCO_2 uptake averaged over the period 1982–2021 (Fig. 1c, d) are similar to the maximum nCO_2 outgassing and aCO_2 uptake anomalies obtained for positive phases of the SAM (Fig. 7a, c), indicating that the positive phases of the SAM simply accentuate the mean SO features (i.e. nCO_2 outgassing gets stronger in outgassing regions). Some of the main areas of nCO_2 outgassing and aCO_2 uptake correspond to major topographic features of the SO: namely, the eastern part of the Southeast Indian Ridge, Drake Passage and the Southwest Indian Ridge (Fig. 1c, d, e). On the contrary, the cyclonic circulation in the relatively deep basin of the eastern part of the Ross Sea and Amundsen–Bellinghousen Sea is associated with nCO_2 uptake. This could be due to enhanced eddy mixing over topography linked to the merging of multiple jets (Lu and Speer, 2010) and warrants further study.

4 Discussion and conclusions

We have used an eddy-rich global ocean, sea-ice, carbon cycle model to assess changes in SO total, natural and anthropogenic CO_2 fluxes over the last 50 years. The multi-decadal strengthening and poleward shift of the SH westerlies, associated with a shift towards positive phases of the SAM during that period, drives a decrease in nCO_2 uptake with a trend of $-0.007 \text{ GtC yr}^{-2}$. On the other hand, the increase in CO_2 growth rate leads to a higher aCO_2 uptake with a trend of $0.014 \text{ GtC yr}^{-2}$. A strengthening and poleward shift of the SH westerlies enhance the aCO_2 uptake, but the magnitude of this change is only 30 % of the associated enhanced nCO_2 outgassing. As a result, while the tCO_2 uptake increases between 1980 and 2021 with a trend of $0.007 \text{ GtC yr}^{-2}$, it

would have likely increased twice as fast without a strengthening and poleward shift of the SH westerlies. These CO_2 flux trends simulated with a high-resolution eddy-rich model are similar to those obtained by a similar simulation performed with ACCESS-OM2 at 1° resolution (Fig. 2), even though the nCO_2 trend is slightly smaller ($-0.005 \text{ GtC yr}^{-2}$) and the tCO_2 trend larger ($0.009 \text{ GtC yr}^{-2}$) in the 1° than the 0.1° experiment. These results are also consistent with those of Lovenduski et al. (2008), who simulated an increase in nCO_2 outgassing between 1979 and 2004 with a trend of $0.004 \text{ GtC yr}^{-2}$, an increase in aCO_2 uptake with a trend of $0.011 \text{ GtC yr}^{-2}$, and, thus, an increase in tCO_2 uptake of $0.007 \text{ GtC yr}^{-2}$ using a coarse-resolution ocean model. The multi-decadal, large-scale oceanic carbon cycle response to a strengthening and poleward shift of the SH westerlies is thus robust from eddy-rich to coarse-resolution models.

In addition, the total air–sea CO_2 fluxes exhibit large ($\sim 0.1 \text{ GtC yr}^{-1}$) decadal-scale variability, thus supporting previous inferences of decadal scale changes in SO CO_2 fluxes (Li and Ilyina, 2018; Lovenduski et al., 2008; Landschützer et al., 2015; Gruber et al., 2019). The simulated variability is not as large as that derived from observational estimates ($\sim 0.25 \text{ GtC yr}^{-1}$) (Landschützer et al., 2016; Bushinsky et al., 2019; Keppler and Landschützer, 2019) but is within the uncertainty band ($\pm 0.15 \text{ GtC yr}^{-1}$) (Gruber et al., 2019; Bushinsky et al., 2019). Such a mismatch between simulated SO tCO_2 variations and observations is prevalent in hindcast simulations (Gruber et al., 2019; Hauck et al., 2020) and could be due to an overestimation of the observed SO CO_2 flux variability (Gloege et al., 2021). The underestimation of the changes in tCO_2 uptake in the simulation could also be due a misrepresentation of Southern Ocean stratification. It has, indeed, been suggested that the overturning rate of the lower cell weakened in the 2000s (DeVries et al., 2017) due to enhanced stratification in the Southern

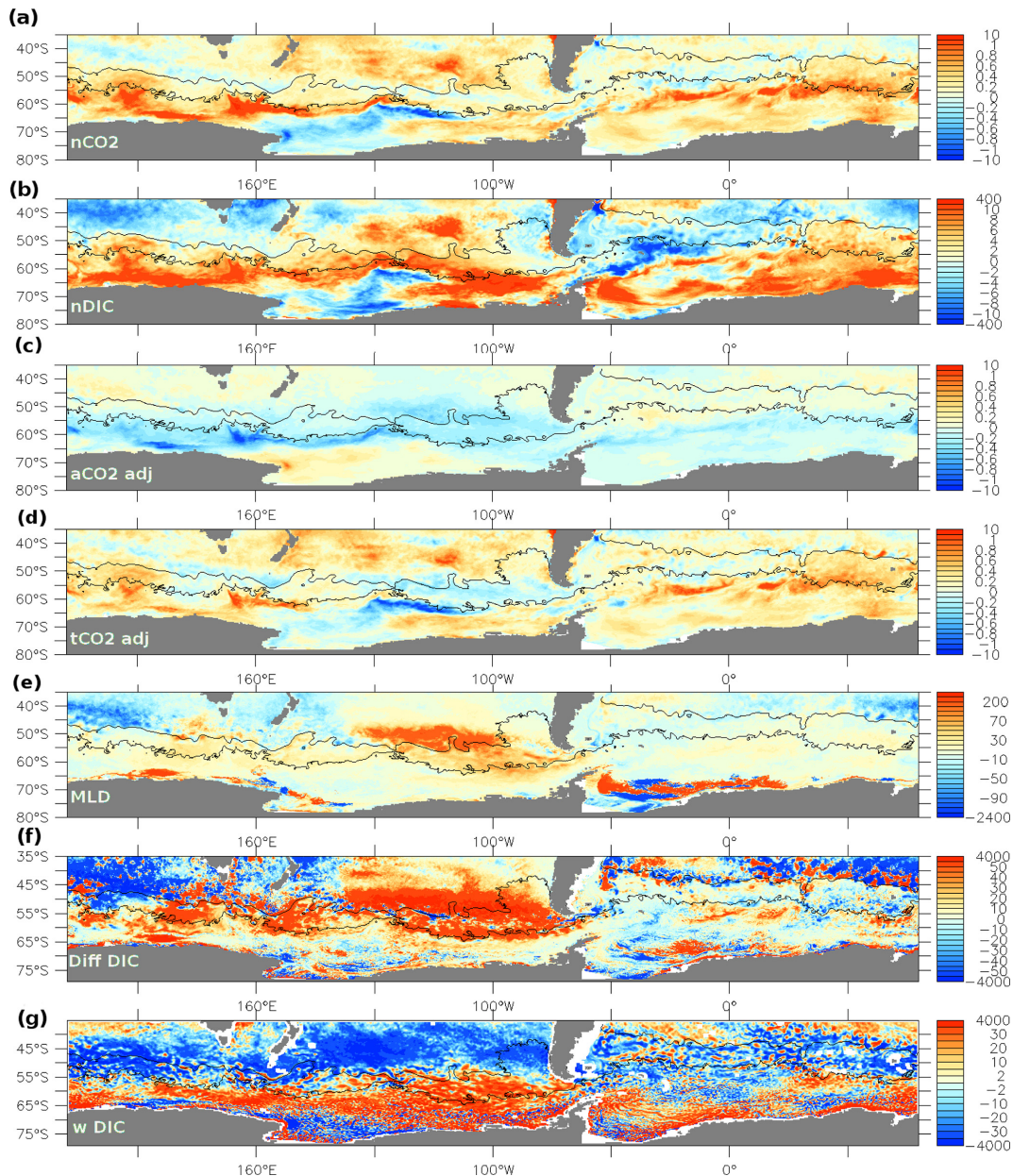


Figure 7. (a) $n\text{CO}_2$ flux ($\text{mol m}^{-2} \text{yr}^{-1}$), (b) surface $n\text{DIC}$ (mmol m^{-3}), (c) adjusted $a\text{CO}_2$ flux ($\text{molC m}^{-2} \text{yr}^{-1}$) and (d) adjusted $t\text{CO}_2$ flux ($\text{molC m}^{-2} \text{yr}^{-1}$) anomalies for a composite of positive phases of the SAM (≥ 0.33 , i.e. 1998, 1999, 2010, 2015, 2021) compared to a composite of negative SAM years (≤ 0.33 , i.e. 1980, 1991, 1992, 2002) for the ACCESS-OM2-01 simulation. Linear trends in $a\text{CO}_2$ fluxes have been removed from the $a\text{CO}_2$ and $t\text{CO}_2$ anomalies to take into account the difference in mean years between the composite of positive and negative SAM years. Annual average anomalies of (e) maximum monthly mixed layer depth (m), (f) vertical diffusivity multiplied by the DIC gradient at the base of mixed layer ($\text{molC m}^{-2} \text{yr}^{-1}$) and (g) vertical Ekman DIC advection with a 21 point spatial smoothing ($\text{molC m}^{-2} \text{yr}^{-1}$), for positive phases of the SAM compared to negative SAM years.

Ocean (de Lavergne et al., 2014), linked to enhanced Antarctic basal melt rates (Adusumilli et al., 2020). Enhanced stratification in the Southern Ocean would weaken the $a\text{CO}_2$ uptake (Bourgeois et al., 2022) but would reduce the $n\text{CO}_2$ outgassing (Menviel et al., 2015), thus potentially enhancing $t\text{CO}_2$ uptake.

To first order, the simulated decadal-scale changes in $t\text{CO}_2$ fluxes are due to changes in $n\text{CO}_2$ fluxes primarily arising from changes in the magnitude of the SH westerlies but are also due to variations in the latitudinal position of the SH winds. While we find a strong link between regional wind changes and $n\text{CO}_2$ and $t\text{CO}_2$ fluxes, we find that minima

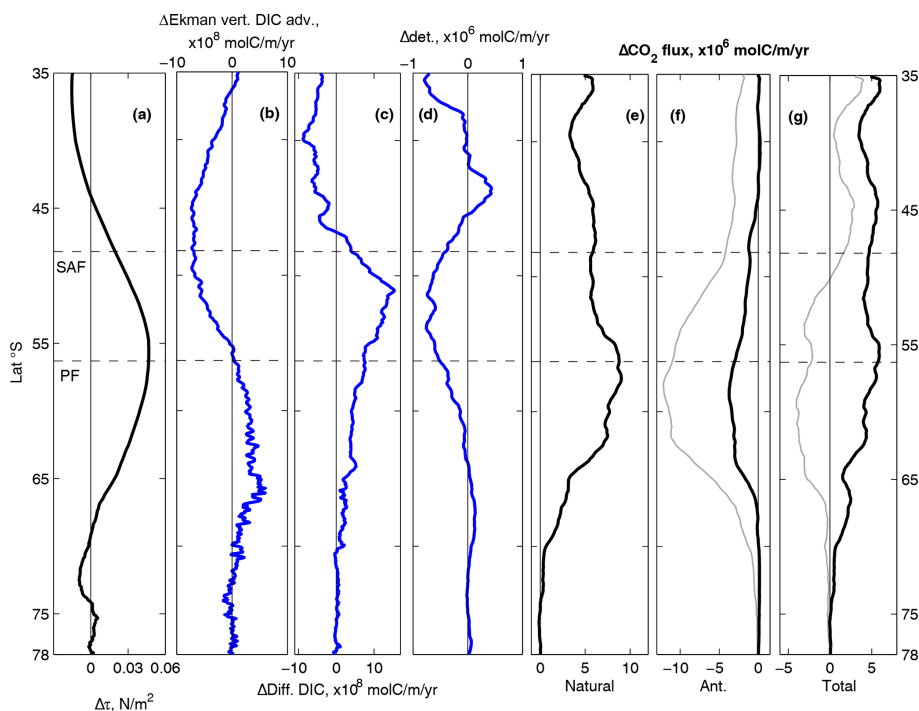


Figure 8. (a) Zonally averaged wind stress anomalies (N m^{-2}); anomalies in zonally integrated (b) vertical Ekman DIC advection ($\times 10^8 \text{ molC m}^{-1} \text{ yr}^{-1}$), (c) vertical diffusivity multiplied by the DIC gradient at the base of mixed layer ($\times 10^8 \text{ molC m}^{-1} \text{ yr}^{-1}$), (d) detritus flux at 100 m depth ($\times 10^6 \text{ molC m}^{-1} \text{ yr}^{-1}$), (e) $n\text{CO}_2$, (f) $a\text{CO}_2$ and (g) $t\text{CO}_2$ fluxes ($\times 10^6 \text{ molC m}^{-1} \text{ yr}^{-1}$) for the positive SAM composite compared to the negative SAM composite in the ACCESS-OM2-01 simulation. In (f) and (g) the grey lines represent the simulated $a\text{CO}_2$ and $t\text{CO}_2$ fields, while the black lines include a correction for the fact that the positive SAM composite represents more recent years than the negative SAM composite. The linear trends in $a\text{CO}_2$ and $t\text{CO}_2$ fluxes between 1980 and 2021 are calculated. The equivalent mean $a\text{CO}_2$ and $t\text{CO}_2$ flux differences between the mean positive and negative SAM composites are then subtracted.

in $t\text{CO}_2$ uptake arise from a strengthening and/or poleward shift of the SH westerlies and thus positive phases of the SAM. This is in contrast to the conclusion of Keppler and Landschützer (2019) that the SAM had a net zero effect on SO $t\text{CO}_2$ uptake. Both our study and the one of Keppler and Landschützer (2019) highlighted enhanced $t\text{CO}_2$ outgassing south of 50°S during positive phases of the SAM, as well as zonal asymmetries with enhanced $t\text{CO}_2$ uptake in the Pacific sector of the SO. While Keppler and Landschützer (2019) suggest this is linked to the zonal wave number 3 pattern, we attribute these asymmetries to the bathymetry and different poleward trends of the westerlies in the different sectors of the SO.

A stagnation of SO $t\text{CO}_2$ uptake between 1980 and 2000 is simulated. This time period corresponds to the largest rate of increase and shift in westerly wind stress. The timing and magnitude of this stagnation in $t\text{CO}_2$ uptake in the SO is in agreement with observational estimates (Lovenduski et al., 2008; Landschützer et al., 2015; Gruber et al., 2019; Keppler and Landschützer, 2019). While the impact of the SAM on SO CO_2 fluxes is clear in our simulation, the early 1990s also feature the lowest atmospheric CO_2 growth rate of the period studied here (McKinley et al., 2020). The simulated

SO $a\text{CO}_2$ uptake in the early 1990s is thus the lowest of the period, noting that positive phases of the SAM are usually associated with slightly enhanced $a\text{CO}_2$ uptake. Our results thus also support the conclusion that the slowdown of the SO $t\text{CO}_2$ uptake in the early 1990s was due to a low atmospheric CO_2 growth rate (McKinley et al., 2020) and not a positive phase of the SAM (LeQuéré et al., 2007; Lovenduski et al., 2008; Matear and Lenton, 2008). In agreement with observations, a re-invigoration of $t\text{CO}_2$ uptake is simulated in the early 2000s (Keppler and Landschützer, 2019), mostly due to a pause in the positive SAM trend. Since the mid 2000s, the $t\text{CO}_2$ uptake has increased slowly, but we find that the reversal in $t\text{CO}_2$ uptake that had been highlighted in the mid 2010s (Keppler and Landschützer, 2019) was short-lived and due to the strong positive 2015 SAM.

The enhanced $n\text{CO}_2$ outgassing during positive phases of the SAM is due to higher surface $n\text{DIC}$ concentration south of the PF, partly compensated by lower SST. This increase in surface $n\text{DIC}$ results from enhanced vertical $n\text{DIC}$ advection, mostly Ekman-driven, as well as enhanced vertical $n\text{DIC}$ diffusion at the base of the mixed layer. This significant role of vertical diffusion is in agreement with a previous study performed with an eddy-permitting model (Dufour

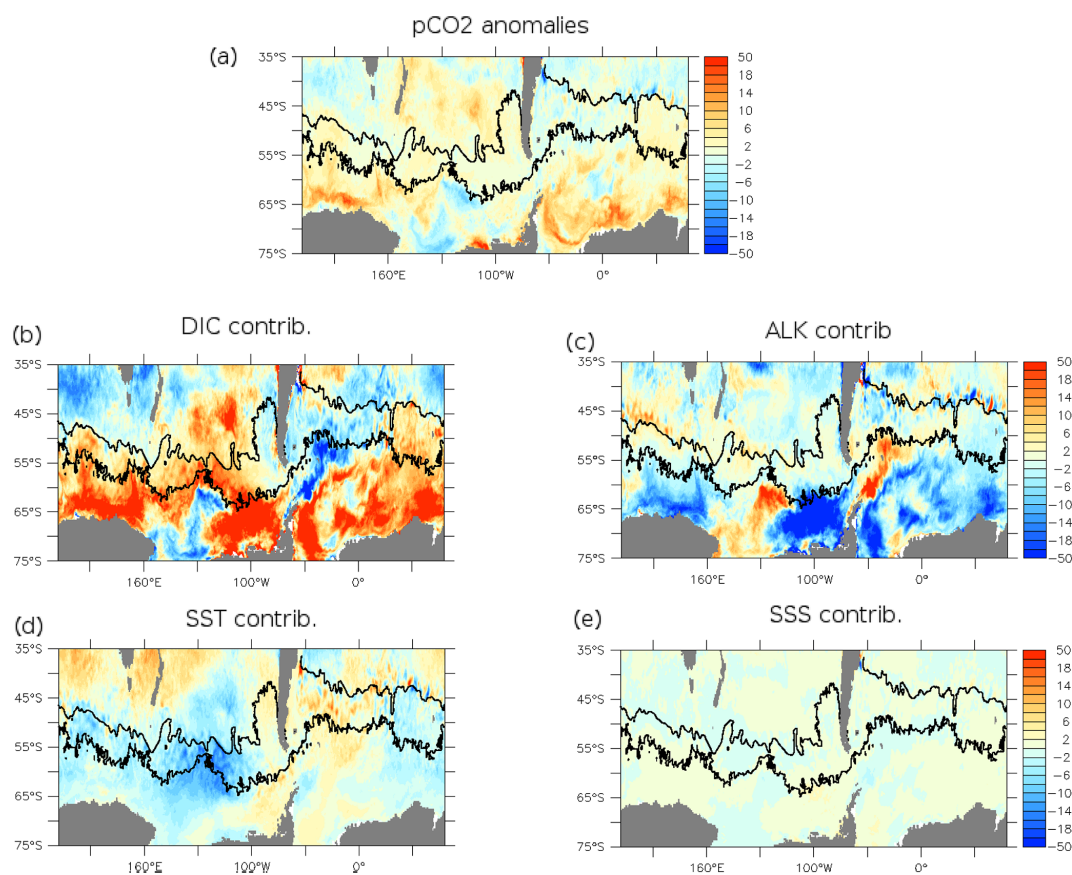


Figure 9. Surface ocean (a) natural $p\text{CO}_2$ anomalies (ppm) for a composite of positive phases of the SAM compared to a composite of negative SAM years (see Fig. 7) and the $p\text{CO}_2$ contributions (ppm) from (b) nDIC, (c) ALK, (d) SST and (e) SSS for the ACCESS-OM2-01 simulation.

et al., 2013), even if contrarily to that study we find an equal weight of vertical advection and Ekman pumping south of the PF. The dominance of Ekman-driven vertical nDIC advection also explains the similar results obtained in the high and coarse-resolution versions of the ACCESS-OM2. As in previous studies, we thus find that changes in oceanic circulation are the primary driver of changes in SO CO₂ fluxes on decadal-time scales (Dufour et al., 2013; Resplandy et al., 2015; Nevison et al., 2020).

Previous studies have suggested that wind-driven changes in oceanic circulation in the Southern Ocean are partially compensated by the eddy-driven transport (Morrison and Hogg, 2013). Similarly, Dufour et al. (2013) suggested that 1/3 of the Ekman-driven DIC transport arising from positive phases of the SAM was compensated by eddy transport. Here, despite a 20% increase in wind stress, only a small ACC increase (134 to 138 Sv) is simulated, thus supporting the eddy saturation theory. Yet, we find that changes in the position and strength of the SH westerlies lead to an outgassing of nCO₂ on a yearly as well as multi-decadal timescale, with an amplitude similar to that found in a similar model (ACCESS-OM2) with a 1° resolution. This is

an important result as it was suggested that mesoscale eddies would compensate for the wind-driven circulation in the Southern Ocean, thus mitigating the carbon cycle response to changes in the strength and position of the westerlies. Here, we show that even in an eddy-rich model, a strengthening and/or a poleward shift of the westerlies leads to enhanced CO₂ outgassing. This further suggests that ocean models with a ~1° resolution correctly capture the large-scale carbon cycle response to changes in the SH westerlies. It should, however, be noted that in the 1° ocean model used here, the GM coefficient varies in space and time (Kiss et al., 2020). While both the 0.1 and 1° resolution simulations display broadly similar mean CO₂ fluxes (Figs. 1 and S4) and CO₂ fluxes response to positive phase of the SAM (Figs. 7 and S8), higher nCO₂ outgassing is simulated south of the PF in the 0.1 than 1° resolution. This could be due to larger upwelling downstream of topographic features in the eddy-rich version of the model.

If SH westerly winds continue to strengthen, as projected under RCP8.5/SSP5-85 scenarios (Große et al., 2020; Goyal et al., 2021), our experiments suggest that the increase in aCO₂ uptake would be partly compensated by nCO₂ out-

gassing, thus leading to only a small increase in tCO₂ uptake. Future changes in SO carbon uptake will, thus, likely result from a fine balance between natural carbon release and anthropogenic carbon uptake, which will itself depend on changes in SH westerlies, SO stratification and temperature, as well as the rate of anthropogenic carbon emissions.

Data availability. The data linked to this study has been deposited on UNSWorks <http://hdl.handle.net/1959.4/101483>, last access: 1 September 2023 under the DOI <https://doi.org/10.26190/unsworks/25190> (Menviel, 2023).

Supplement. The supplement related to this article is available online at: <https://doi.org/10.5194/bg-20-4413-2023-supplement>.

Author contributions. LCM designed the study with PS and DW. AEK, MAC and HH developed some parts of the model and ran the experiment in collaboration with the COSIMA consortium. LCM analysed the data and wrote the manuscript with contributions from all authors.

Competing interests. The contact author has declared that none of the authors has any competing interests.

Disclaimer. Publisher's note: Copernicus Publications remains neutral with regard to jurisdictional claims made in the text, published maps, institutional affiliations, or any other geographical representation in this paper. While Copernicus Publications makes every effort to include appropriate place names, the final responsibility lies with the authors.

Acknowledgements. The authors thank the Consortium for Ocean-Sea Ice Modelling in Australia (COSIMA; <http://www.cosima.org.au>, last access: 1 September 2023) for making the ACCESS-OM2 suite of models available at <https://github.com/COSIMA/access-om2>, last access: 1 September 2023. Model runs were undertaken with the assistance of resources from the National Computational Infrastructure (NCI), which is supported by the Australian Government. The authors thank Kial Stewart for sharing the code to calculate the SAM index from the JRA-55do dataset.

Financial support. This research has been supported by the Australian Research Council (grant nos. FT180100606, FT190100413, SR200100008, LP160100073 and LP200100406) and the Australian Government's Australian Antarctic Science Program (grant no. 4541).

Review statement. This paper was edited by Peter Landschützer and reviewed by two anonymous referees.

References

- Adusumilli, S., Fricker, H., Medley, B., Padman, L., and Siegfried, M.: Interannual variations in meltwater input to the Southern Ocean from Antarctic ice shelves, *Nat. Geosci.*, 13, 616–620, <https://doi.org/10.1038/s41561-020-0616-z>, 2020.
- Arblaster, J. M. and Meehl, G. A.: Contributions of External Forcings to Southern Annular Mode Trends, *J. Clim.*, 19, 2896–2905, <https://doi.org/10.1175/JCLI3774.1>, 2006.
- Bakker, D. C. E., Pfeil, B., Landa, C. S., Metz, N., O'Brien, K. M., Olsen, A., Smith, K., Cosca, C., Harasawa, S., Jones, S. D., Nakaoka, S., Nojiri, Y., Schuster, U., Steinhoff, T., Sweeney, C., Takahashi, T., Tilbrook, B., Wada, C., Wanninkhof, R., Alin, S. R., Balestrini, C. F., Barbero, L., Bates, N. R., Bianchi, A. A., Bonou, F., Boutin, J., Bozec, Y., Burger, E. F., Cai, W.-J., Castle, R. D., Chen, L., Chierici, M., Currie, K., Evans, W., Featherstone, C., Feely, R. A., Fransson, A., Goyet, C., Greenwood, N., Gregor, L., Hankin, S., Hardman-Mountford, N. J., Harlay, J., Hauck, J., Hoppema, M., Humphreys, M. P., Hunt, C. W., Huss, B., Ibáñez, J. S. P., Johannessen, T., Keeling, R., Kitidis, V., Körtzinger, A., Kozyr, A., Krasakopoulou, E., Kuwata, A., Landschützer, P., Lauvset, S. K., Lefèvre, N., Lo Monaco, C., Manke, A., Mathis, J. T., Merlivat, L., Millero, F. J., Monteiro, P. M. S., Munro, D. R., Murata, A., Newberger, T., Omar, A. M., Ono, T., Paterson, K., Pearce, D., Pierrot, D., Robbins, L. L., Saito, S., Salisbury, J., Schlitzer, R., Schneider, B., Schweitzer, R., Sieger, R., Skjelvan, I., Sullivan, K. F., Sutherland, S. C., Sutton, A. J., Tadokoro, K., Telszewski, M., Tuma, M., van Heuven, S. M. A. C., Vandemark, D., Ward, B., Watson, A. J., and Xu, S.: A multi-decade record of high-quality *f*CO₂ data in version 3 of the Surface Ocean CO₂ Atlas (SOCAT), *Earth Syst. Sci. Data*, 8, 383–413, <https://doi.org/10.5194/essd-8-383-2016>, 2016.
- Banerjee, A., Fyfe, J., Polvani, L., Waugh, D., and Chang, K.-L.: A pause in Southern Hemisphere circulation trends due to the Montreal Protocol, *Nature*, 579, 544–548, <https://doi.org/10.1038/s41586-020-2120-4>, 2020.
- Bourgeois, T., Goris, N., Schwinger, J., and Tjiputra, J.: Stratification constrains future heat and carbon uptake in the Southern Ocean between 30° S and 55° S, *Nat. Commun.*, 13, 340, <https://doi.org/10.1038/s41467-022-27979-5>, 2022.
- Broecker, W., Takahashi, T., Simpson, H., and Peng, T.-H.: Fate of fossil fuel carbon dioxide and the global carbon budget, *Science*, 206, 409–418, <https://doi.org/10.1126/science.206.4417.409>, 1979.
- Bushinsky, S. M., Landschützer, P., Rödenbeck, C., Gray, A. R., Baker, D., Mazloff, M. R., Resplandy, L., Johnson, K. S., and Sarmiento, J. L.: Reassessing Southern Ocean Air-Sea CO₂ Flux Estimates With the Addition of Biogeochemical Float Observations, *Global Biogeochem. Cy.*, 33, 1370–1388, <https://doi.org/10.1029/2019GB006176>, 2019.
- de Lavergne, C., Palter, J., Galbraith, E., Bernardello, R., and Marinov, I.: Cessation of deep convection in the open Southern Ocean under anthropogenic climate change, *Nat. Clim. Change*, 4, 278–282, <https://doi.org/10.1038/NCLIMATE2132>, 2014.
- DeVries, T., Holzer, M., and Primeau, F.: Recent increase in oceanic carbon uptake driven by weaker upper-ocean overturning, *Nature*, 542, 215–218, <https://doi.org/10.1038/nature21068>, 2017.
- Dufour, C. O., Sommer, J. L., Zika, J., Gehlen, M., Orr, J., Mathiot, J., and Barnier, B.: Standing and Transient Eddies in the Re-

- sponse of the Southern Ocean Meridional Overturning to the Southern Annular Mode, *J. Clim.*, 25, 6958–6974, 2012.
- Dufour, C. O., Sommer, J. L., Gehlen, M., Orr, J. C., Molines, J.-M., Simeon, J., and Barnier, B.: Eddy compensation and controls of the enhanced sea-to-air CO₂ flux during positive phases of the Southern Annular Mode, *Global Biogeochem. Cy.*, 27, 950–961, <https://doi.org/10.1002/gbc.20090>, 2013.
- Farneti, R., Delworth, T., Rosati, A., Griffies, S., and Zeng, F.: The role of mesoscale eddies in the rectification of the Southern Ocean response to climate change, *J. Phys. Oceanogr.*, 40, 1539–1557, 2010.
- Fogt, R. L. and Marshall, G. J.: The Southern Annular Mode: Variability, trends, and climate impacts across the Southern Hemisphere, *WIREs Clim. Change*, 11, e652, <https://doi.org/10.1002/wcc.652>, 2020.
- Friedlingstein, P., Jones, M. W., O’Sullivan, M., Andrew, R. M., Bakker, D. C. E., Hauck, J., Le Quéré, C., Peters, G. P., Peters, W., Pongratz, J., Sitch, S., Canadell, J. G., Ciais, P., Jackson, R. B., Alin, S. R., Anthoni, P., Bates, N. R., Becker, M., Belouin, N., Bopp, L., Chau, T. T. T., Chevallier, F., Chini, L. P., Cronin, M., Currie, K. I., Decharme, B., Djetchouang, L. M., Dou, X., Evans, W., Feely, R. A., Feng, L., Gasser, T., Gilfillan, D., Gkritzalis, T., Grassi, G., Gregor, L., Gruber, N., Gürses, O., Harris, I., Houghton, R. A., Hurtt, G. C., Iida, Y., Ilyina, T., Luijkx, I. T., Jain, A., Jones, S. D., Kato, E., Kennedy, D., Klein Goldewijk, K., Knauer, J., Korsbakken, J. I., Körtzinger, A., Landschützer, P., Lauvset, S. K., Lefèvre, N., Lienert, S., Liu, J., Marland, G., McGuire, P. C., Melton, J. R., Munro, D. R., Nabel, J. E. M. S., Nakaoka, S.-I., Niwa, Y., Ono, T., Pierrot, D., Poulter, B., Rehder, G., Resplandy, L., Robertson, E., Rödenbeck, C., Rosan, T. M., Schwinger, J., Schwingshackl, C., Séférian, R., Sutton, A. J., Sweeney, C., Tanhua, T., Tans, P. P., Tian, H., Tilbrook, B., Tubiello, F., van der Werf, G. R., Vuichard, N., Wada, C., Wanninkhof, R., Watson, A. J., Willis, D., Wiltshire, A. J., Yuan, W., Yue, C., Yue, X., Zaehle, S., and Zeng, J.: Global Carbon Budget 2021, *Earth Syst. Sci. Data*, 14, 1917–2005, <https://doi.org/10.5194/essd-14-1917-2022>, 2022.
- Gent, P. and McWilliams, J.: Isopycnal mixing in ocean circulation models, *J. Phys. Oceanogr.*, 20, 150–155, 1990.
- Gloege, L., McKinley, G. A., Landschützer, P., Fay, A. R., Fräñzlicher, T. L., Fyfe, J. C., Ilyina, T., Jones, S., Lovenduski, N. S., Rodgers, K. B., Schlunegger, S., and Takano, Y.: Quantifying Errors in Observationally Based Estimates of Ocean Carbon Sink Variability, *Global Biogeochem. Cy.*, 35, e2020GB006788, <https://doi.org/10.1029/2020GB006788>, 2021.
- Goyal, R., Sen Gupta, A., Jucker, M., and England, M. H.: Historical and Projected Changes in the Southern Hemisphere Surface Westerlies, *Geophys. Res. Lett.*, 48, e2020GL090849, <https://doi.org/10.1029/2020GL090849>, 2021.
- Gregor, L., Kok, S., and Monteiro, P. M. S.: Interannual drivers of the seasonal cycle of CO₂ in the Southern Ocean, *Biogeosciences*, 15, 2361–2378, <https://doi.org/10.5194/bg-15-2361-2018>, 2018.
- Griffies, S.: Elements of the Modular Ocean Model (MOM), GFDL Ocean Group Tech. Rep., 7, 618 pp., 2012.
- Grose, M. R., Narsey, S., Delage, F. P., Dowdy, A. J., Bador, M., Boschat, G., Chung, C., Kajtar, J. B., Rauniyar, S., Freund, M. B., Lyu, K., Rashid, H., Zhang, X., Wales, S., Trenham, C., Holbrook, N. J., Cowan, T., Alexander, L., Arblaster, J. M., and Power, S.: Insights From CMIP6 for Australia’s Future Climate, *Earth’s Future*, 8, e2019EF001469, <https://doi.org/10.1029/2019EF001469>, 2020.
- Gruber, N., Landschützer, P., and Lovenduski, N.: The variable Southern Ocean carbon sink, *Ann. Rev. Mar. Sci.*, 11, 159–186, 2019.
- Gruber, N., Bakker, D., DeVries, T., Gregor, L., Hauck, J., Landschützer, P., McKinley, G., and Müller, J.: Trends and variability in the ocean carbon sink, *Nat. Rev. Earth Environ.*, 4, 119–134, <https://doi.org/10.1038/s43017-022-00381-x>, 2023.
- Hallberg, R. and Gnanadesikan, A.: The role of eddies in determining the structure and response of the wind-driven southern hemisphere overturning: Results from the modeling eddies in the Southern Ocean (MESO) project, *J. Phys. Oceanogr.*, 36, 2232–2252, 2006.
- Hauck, J., Völker, C., Wang, T., Hoppema, M., Losch, M., and Wolf-Gladrow, D. A.: Seasonally different carbon flux changes in the Southern Ocean in response to the southern annular mode, *Global Biogeochem. Cy.*, 27, 1236–1245, <https://doi.org/10.1002/2013GB004600>, 2013.
- Hauck, J., Zeising, M., Le Quéré, C., Gruber, N., Bakker, D. C. E., Bopp, L., Chau, T. T. T., Gürses, A., Ilyina, T., Landschützer, P., Lenton, A., Resplandy, L., Rödenbeck, C., Schwinger, J., and Séférian, R.: Consistency and Challenges in the Ocean Carbon Sink Estimate for the Global Carbon Budget, *Front. Mar. Sci.*, 7, 571720, <https://doi.org/10.3389/fmars.2020.571720>, 2020.
- Hayashida, H., Jin, M., Steiner, N. S., Swart, N. C., Watanabe, E., Fiedler, R., Hogg, A. M., Kiss, A. E., Matear, R. J., and Strutton, P. G.: Ice Algae Model Intercomparison Project phase 2 (IAMIP2), *Geosci. Model Dev.*, 14, 6847–6861, <https://doi.org/10.5194/gmd-14-6847-2021>, 2021.
- Hunke, E., Lipscomb, W., Jones, P., Turner, A., Jeffery, N., and Elliott, S.: CICE, The Los Alamos Sea Ice Model, <https://www.osti.gov/biblio/1364126> (1 September 2022), 2017.
- Joos, F. and Spahni, R.: Rates of change in natural and anthropogenic radiative forcing over the past 20,000 years, *P. Natl. Acad. Sci. USA*, 105, 1425–1430, <https://doi.org/10.1073/pnas.0707386105>, 2008.
- Kepler, L. and Landschützer, P.: Regional Wind Variability Modulates the Southern Ocean Carbon Sink, *Sci. Rep.*, 9, 7384, <https://doi.org/10.1038/s41598-019-43826-y>, 2019.
- Kidston, M., Matear, R., and Baird, M.: Parameter optimisation of a marine ecosystem model at two contrasting stations in the Sub-Antarctic Zone, *Deep-Sea Res. Pt. II*, 58, 2301–2315, 2011.
- Kiss, A. E., Hogg, A. M., Hannah, N., Boeira Dias, F., Brassington, G. B., Chamberlain, M. A., Chapman, C., Dobrohotoff, P., Domingues, C. M., Duran, E. R., England, M. H., Fiedler, R., Griffies, S. M., Heerdegen, A., Heil, P., Holmes, R. M., Klocker, A., Marsland, S. J., Morrison, A. K., Munroe, J., Nikurashin, M., Oke, P. R., Pilo, G. S., Richet, O., Savita, A., Spence, P., Stewart, K. D., Ward, M. L., Wu, F., and Zhang, X.: ACCESS-OM2 v1.0: a global ocean–sea ice model at three resolutions, *Geosci. Model Dev.*, 13, 401–442, <https://doi.org/10.5194/gmd-13-401-2020>, 2020.
- Landschützer, P., Gruber, N., Haumann, F. A., Rödenbeck, C., Bakker, D. C. E., van Heuven, S., Hoppema, M., Metzl, N., Sweeney, C., Takahashi, T., Tilbrook, B., and Wanninkhof, R.: The reinvigoration of the Southern Ocean carbon sink, *Science*, 349, 1221–1224, <https://doi.org/10.1126/science.aab2620>, 2015.

- Landschützer, P., Gruber, N., and Bakker, D. C. E.: Decadal variations and trends of the global ocean carbon sink, *Global Biogeochem. Cy.*, 30, 1396–1417, <https://doi.org/10.1002/2015GB005359>, 2016.
- Landschützer, P., Bushinsky, S. M., and Gray, A. R.: A combined globally mapped CO₂ flux estimate based on the Surface Ocean CO₂ Atlas Database (SOCAT) and Southern Ocean Carbon and Climate Observations and Modeling (SOCCOM) biogeochemistry floats from 1982 to 2017, Dataset, NOAA National Centers for Environmental Information, <https://doi.org/10.25921/9hsn-xq82>, 2019.
- Landschützer, P., Gruber, N., and Bakker, D.: An observation-based global monthly gridded sea surface pCO₂ product from 1982 onward and its monthly climatology (NCEI Accession 0160558), Version 5.5., Dataset, NOAA National Centers for Environmental Information, <https://doi.org/10.7289/V5Z899N6>, 2020.
- Large, W. and Yeager, S.: The global climatology of an interannually varying air-sea flux data set, *Clim. Dynam.*, 33, 341–364, 2009.
- Lauderdale, J. M., Garabato, A. C. N., Oliver, K. I. C., Follows, M. J., and Williams, R. G.: Wind-driven changes in Southern Ocean residual circulation, ocean carbon reservoirs and atmospheric CO₂, *Clim. Dynam.*, 41, 2145–2164, <https://doi.org/10.1007/s00382-012-1650-3>, 2013.
- Lauderdale, J. M., Williams, R. G., Munday, D. R., and Marshall, D. P.: The impact of Southern Ocean residual upwelling on atmospheric CO₂ on centennial and millennial timescales, *Clim. Dynam.*, 48, 1611–1631, <https://doi.org/10.1007/s00382-016-3163-y>, 2017.
- Law, R. M., Ziehn, T., Matear, R. J., Lenton, A., Chamberlain, M. A., Stevens, L. E., Wang, Y. P., Srbinovsky, J., Bi, D., Yan, H., and Vohralik, P. F.: The carbon cycle in the Australian Community Climate and Earth System Simulator (ACCESS-ESM1) – Part I: Model description and pre-industrial simulation, *Geosci. Model Dev.*, 10, 2567–2590, <https://doi.org/10.5194/gmd-10-2567-2017>, 2017.
- Le Quéré, C., Andrew, R. M., Friedlingstein, P., Sitch, S., Pongratz, J., Manning, A. C., Korsbakken, J. I., Peters, G. P., Canadell, J. G., Jackson, R. B., Boden, T. A., Tans, P. P., Andrews, O. D., Arora, V. K., Bakker, D. C. E., Barbero, L., Becker, M., Betts, R. A., Bopp, L., Chevallier, F., Chini, L. P., Ciais, P., Cosca, C. E., Cross, J., Currie, K., Gasser, T., Harris, I., Hauck, J., Haverd, V., Houghton, R. A., Hunt, C. W., Hurtt, G., Ilyina, T., Jain, A. K., Kato, E., Kautz, M., Keeling, R. F., Klein Goldewijk, K., Körtzinger, A., Landschützer, P., Lefèvre, N., Lenton, A., Lienert, S., Lima, I., Lombardozzi, D., Metzl, N., Millero, F., Monteiro, P. M. S., Munro, D. R., Nabel, J. E. M. S., Nakaoka, S.-I., Nojiri, Y., Padin, X. A., Pregon, A., Pfeil, B., Pierrot, D., Poulter, B., Rehder, G., Reimer, J., Rödenbeck, C., Schwinger, J., Séférian, R., Skjelvan, I., Stocker, B. D., Tian, H., Tilbrook, B., Tubiello, F. N., van der Laan-Luijkx, I. T., van der Werf, G. R., van Heuven, S., Viovy, N., Vuichard, N., Walker, A. P., Watson, A. J., Wiltshire, A. J., Zaehle, S., and Zhu, D.: Global Carbon Budget 2017, *Earth Syst. Sci. Data*, 10, 405–448, <https://doi.org/10.5194/essd-10-405-2018>, 2018.
- Lenton, A. and Matear, R.: Role of the Southern Annular Mode (SAM) in Southern Ocean CO₂ uptake, *Global Biogeochem. Cy.*, 21, GB2016, <https://doi.org/10.1029/2006GB002714>, 2007.
- LeQuéré, C., Rödenbeck, C., Buitenhuis, E., Conway, T., Langenfelds, R., Gomez, A., Labuschagne, C., Ramonet, M., Nakazawa, T., Metzl, N., Gillett, N., and Heimann, M.: Saturation of the Southern Ocean CO₂ sink due to recent climate change, *Science*, 316, 1735–1738, 2007.
- Li, H. and Ilyina, T.: Current and Future Decadal Trends in the Oceanic Carbon Uptake Are Dominated by Internal Variability, *Geophys. Res. Lett.*, 45, 916–925, <https://doi.org/10.1002/2017GL075370>, 2018.
- Locarnini, R., Mishonov, A., Antonov, J., Boyer, T., Garcia, H., Baranova, O. K., Zweng, M. M., Paver, C. R., Reagan, J. R., Johnson, D. R., Hamilton, M., and Seidov, D.: World Ocean Atlas 2013, Vol. 1, chap. Temperature, U.S. Government Printing Office, Washington, edited by: Mishonov, A., Technical Ed., NOAA Atlas NESDIS 73, 40 pp., 2013.
- Lovenduski, N., Gruber, N., Doney, S., and Lima, I.: Enhanced CO₂ outgassing in the Southern Ocean from a positive phase of the Southern Annular Mode, *Global Biogeochem. Cy.*, 21, GB2026, <https://doi.org/10.1029/2006GB002900>, 2007.
- Lovenduski, N., Gruber, N., and Doney, S.: Toward a mechanistic understanding of the decadal trends in the Southern Ocean carbon sink, *Global Biogeochem. Cy.*, 22, GB3016, <https://doi.org/10.1029/2007GB003139>, 2008.
- Lu, J. and Speer, K.: Topography, jets, and eddy mixing in the Southern Ocean, *J. Mar. Res.*, 68, 479–502, <https://doi.org/10.1357/002224010794657227>, 2010.
- Mackallah, C., Chamberlain, M., Law, R., Dix, M., Ziehn, T., Bi, D., Bodman, R., Brown, J., Dobrohotoff, P., Druken, K., Evans, B., Harman, I., Hayashida, H., Holmes, R., Kiss, A., Lenton, A., Liu, Y., Marsland, S., Meissner, K., Menviel, L., O’Farrell, S., Rashid, H., Ridzwan, S., Savita, A., Srbinovsky, J., Sullivan, A., Trenham, C., Vohralik, P., Wang, Y.-P., Williams, G., Woodhouse, M., and Yeung, N.: ACCESS datasets for CMIP6: methodology and idealised experiments, *J. Southern Hemis. Earth Syst. Sci.*, 72, 93–116, <https://doi.org/10.1071/ES21031>, 2022.
- Marshall, G.: Trends in the Southern Annular Mode from observations and reanalyses, *J. Clim.*, 16, 4134–4143, 2003.
- Matear, R. and Lenton, A.: Impact of Historical Climate Change on the Southern Ocean Carbon Cycle, *J. Clim.*, 21, 5820–5834, <https://doi.org/10.1175/2008JCLI2194.1>, 2008.
- McKinley, G. A., Fay, A. R., Eddebar, Y. A., Gloege, L., and Lovenduski, N. S.: External Forcing Explains Recent Decadal Variability of the Ocean Carbon Sink, *AGU Adv.*, 1, e2019AV000149, <https://doi.org/10.1029/2019AV000149>, 2020.
- Menviel, L.: Southern Ocean CO₂ fluxes as simulated by the ACCESS-OM2-01 forced with the JRA55-do between 1980 and 2021, UNSW Sydney Library [data set], <https://doi.org/10.26190/unsworks/25190>, 2023.
- Menviel, L., Timmermann, A., Mouchet, A., and Timm, O.: Climate and marine carbon cycle response to changes in the strength of the southern hemispheric westerlies, *Paleoceanography*, 23, PA4201, <https://doi.org/10.1029/2007PA001604>, 2008.
- Menviel, L., Mouchet, A., Meissner, K., Joos, F., and England, M.: Impact of oceanic circulation changes on atmospheric δ¹³CO₂, *Global Biogeochem. Cy.*, 29, 1944–1961, <https://doi.org/10.1002/2015GB005207>, 2015.
- Menviel, L., Spence, P., Yu, J., Chamberlain, M., Matear, R., Meissner, K., and England, M.: Southern Hemisphere wester-

- lies as a driver of the early deglacial atmospheric CO₂ rise, *Nat. Commun.*, 9, 2503, <https://doi.org/10.1038/s41467-018-04876-4>, 2018.
- Mikaloff-Fletcher, S., Gruber, N., Jacobson, A., Doney, S., Dutkiewicz, S., Gerber, M., Follows, M., Joos, F., Lindsay, K., Menemenlis, D., Mouchet, A., Müller, S., and Sarmiento, J.: Inverse estimates of anthropogenic CO₂ uptake, transport, and storage by the ocean, *Global Biogeochem. Cy.*, 20, GB2002, <https://doi.org/10.1029/2005GB002530>, 2006.
- Morrison, A. and Hogg, A.: On the Relationship between Southern Ocean Overturning and ACC Transport, *J. Phys. Oceanogr.*, 43, 140–148, <https://doi.org/10.1175/JPO-D-12-057.1>, 2013.
- Morrison, A. K., Hogg, A. M., England, M. H., and Spence, P.: Warm Circumpolar Deep Water transport toward Antarctica driven by local dense water export in canyons, *Sci. Adv.*, 6, eaav2516, <https://doi.org/10.1126/sciadv.aav2516>, 2020.
- Munday, D. R., Johnson, H. L., and Marshall, D. P.: Eddy Saturation of Equilibrated Circumpolar Currents, *J. Phys. Oceanogr.*, 43, 507–532, <https://doi.org/10.1175/JPO-D-12-095.1>, 2013.
- Munday, D. R., Johnson, H. L., and Marshall, D. P.: Impacts and effects of mesoscale ocean eddies on ocean carbon storage and atmospheric pCO₂, *Global Biogeochem. Cy.*, 28, 877–896, <https://doi.org/10.1002/2014GB004836>, 2014.
- Nevison, C. D., Munro, D. R., Lovenduski, N. S., Keeling, R. F., Manizza, M., Morgan, E. J., and Rödenbeck, C.: Southern Annular Mode Influence on Wintertime Ventilation of the Southern Ocean Detected in Atmospheric O₂ and CO₂ Measurements, *Geophys. Res. Lett.*, 47, e2019GL085667, <https://doi.org/10.1029/2019GL085667>, 2020.
- Oke, P., Griffin, D., Schiller, A., Matear, R., Fiedler, R., Mansbridge, J., Lenton, A., Cahill, M., Chamberlain, M., and Ridgway, K.: Evaluation of a near-global eddy-resolving ocean model, *Geosci. Model Dev.*, 6, 591–615, <https://doi.org/10.5194/gmd-6-591-2013>, 2013.
- Olsen, A., Key, R. M., van Heuven, S., Lauvset, S. K., Velo, A., Lin, X., Schirnick, C., Kozyr, A., Tanhua, T., Hoppema, M., Jutterström, S., Steinfeldt, R., Jeansson, E., Ishii, M., Pérez, F. F., and Suzuki, T.: The Global Ocean Data Analysis Project version 2 (GLODAPv2) – an internally consistent data product for the world ocean, *Earth Syst. Sci. Data*, 8, 297–323, <https://doi.org/10.5194/essd-8-297-2016>, 2016.
- Orr, J. C., Najjar, R. G., Aumont, O., Bopp, L., Bullister, J. L., Danabasoglu, G., Doney, S. C., Dunne, J. P., Dutay, J.-C., Graven, H., Griffies, S. M., John, J. G., Joos, F., Levin, I., Lindsay, K., Matear, R. J., McKinley, G. A., Mouchet, A., Oschlies, A., Romanou, A., Schlitzer, R., Tagliabue, A., Tanhua, T., and Yool, A.: Biogeochemical protocols and diagnostics for the CMIP6 Ocean Model Intercomparison Project (OMIP), *Geosci. Model Dev.*, 10, 2169–2199, <https://doi.org/10.5194/gmd-10-2169-2017>, 2017.
- Resplandy, L., Séférian, R., and Bopp, L.: Natural variability of CO₂ and O₂ fluxes: What can we learn from centuries-long climate models simulations?, *J. Geophys. Res.-Ocean.*, 120, 384–404, <https://doi.org/10.1002/2014JC010463>, 2015.
- Ritter, R., Landschützer, P., Gruber, N., Fay, A. R., Iida, Y., Jones, S., Nakaoka, S., Park, G.-H., Peylin, P., Rödenbeck, C., Rodgers, K. B., Shutler, J. D., and Zeng, J.: Observation-Based Trends of the Southern Ocean Carbon Sink, *Geophys. Res. Lett.*, 44, 12339–12348, <https://doi.org/10.1002/2017GL074837>, 2017.
- Sabine, C., Feely, R., Gruber, N., Key, R., Lee, K., Bullister, J., Wanninkhof, R., Wong, C., Wallace, D., Tilbrook, B., Millero, F., Peng, T.-H., Kozyr, A., Ono, T., and Rios, A.: The oceanic sink of anthropogenic CO₂, *Science*, 305, 367–371, 2004.
- Sarmiento, J. and Gruber, N.: *Ocean Biogeochemical Dynamics*, vol. 526, 503 pp., Princeton, Woodstock, Princeton University Press, 2006.
- Sokolov, S. and Rintoul, S. R.: Circumpolar structure and distribution of the Antarctic Circumpolar Current fronts: 1. Mean circumpolar paths, *J. Geophys. Res.-Ocean.*, 114, C1108, <https://doi.org/10.1029/2008JC005108>, 2009.
- Solodoch, A., Stewart, A. L., Hogg, A. M., Morrison, A. K., Kiss, A. E., Thompson, A. F., Purkey, S. G., and Cimoli, L.: How Does Antarctic Bottom Water Cross the Southern Ocean?, *Geophys. Res. Lett.*, 49, e2021GL097211, <https://doi.org/10.1029/2021GL097211>, 2022.
- Spence, P., Fyfe, J. C., Montenegro, A., and Weaver, A. J.: Southern Ocean response to strengthening winds in an eddy-permitting global climate model, *J. Clim.*, 23, 5332–5343, <https://doi.org/10.1175/2010JCLI3098.1>, 2010.
- Stewart, K. D., Hogg, A., England, M. H., and Waugh, D. W.: Response of the Southern Ocean Overturning Circulation to Extreme Southern Annular Mode Conditions, *Geophys. Res. Lett.*, 47, e2020GL091103, <https://doi.org/10.1029/2020GL091103>, 2020.
- Tagliabue, A., Aumont, O., DeAth, R., Dunne, J. P., Dutkiewicz, S., Galbraith, E., Misumi, K., Moore, J. K., Ridgwell, A., Sherman, E., Stock, C., Vichi, M., Völker, C., and Yool, A.: How well do global ocean biogeochemistry models simulate dissolved iron distributions?, *Global Biogeochem. Cy.*, 30, 149–174, <https://doi.org/10.1002/2015GB005289>, 2016.
- Takahashi, T., Olafsson, J., Goddard, J., Chipman, D., and Sutherland, S.: Seasonal-variation of CO₂ and nutrients in the high-latitude surface oceans – A comparative-study, *Global Biogeochem. Cy.*, 7, 843–878, 1993.
- Takahashi, T., Sutherland, S., Sweeney, C., Poisson, A., Metzl, N., Tilbrook, B., Bates, N., Wanninkhof, R., Feely, R., Sabine, C., Olafsson, J., and Nojiri, Y.: Global sea-air CO₂ flux based on climatological surface ocean pCO₂ and seasonal biological and temperature effects, *Deep-Sea Res. Pt. II*, 49, 1601–1622, 2002.
- Takahashi, T., Sutherland, S. C., Wanninkhof, R., Sweeney, C., Feely, R. A., Chipman, D. W., Hales, B., Friederich, G., Chavez, F., Sabine, C., Watson, A., Bakker, D. C., Schuster, U., Metzl, N., Yoshikawa-Inoue, H., Ishii, M., Midorikawa, T., Nojiri, Y., Körtzinger, A., Steinhoff, T., Hoppema, M., Olafsson, J., Arnarson, T. S., Tilbrook, B., Johannessen, T., Olsen, A., Bellerby, R., Wong, C., Delille, B., Bates, N., and de Baar, H. J.: Climatological mean and decadal change in surface ocean pCO₂, and net sea-air CO₂ flux over the global oceans, *Deep-Sea Res. Pt. II*, 56, 554–577, <https://doi.org/10.1016/j.dsr2.2008.12.009>, 2009.
- Thompson, D. and Solomon, S.: Interpretation of recent southern hemisphere climate change, *Science*, 296, 895–899, 2002.
- Thompson, D., Solomon, S., Kushner, P., England, M., Grise, K., and Karoly, D.: Signatures of the Antarctic ozone hole in Southern Hemisphere surface climate change, *Nat. Geosci.*, 4, 741–749, <https://doi.org/10.1038/ngeo1296>, 2011.
- Toggweiler, J.: Variation of atmospheric CO₂ by ventilation of the ocean's deepest water, *Paleoceanography*, 14, 571–588, 1999.

- Tsujino, H., Urakawa, S., Nakano, H., Small, R. J., Kim, W. M., Yeager, S. G., Danabasoglu, G., Suzuki, T., Bamber, J. L., Bentsen, M., BÅ¶ning, C. W., Bozec, A., Chassignet, E. P., Curchitser, E., Boeira Dias, F., Durack, P. J., Griffies, S. M., Harada, Y., Ilicak, M., Josey, S. A., Kobayashi, C., Kobayashi, S., Komuro, Y., Large, W. G., Le Sommer, J., Marsland, S. J., Masina, S., Scheinert, M., Tomita, H., Valdivieso, M., and Yamazaki, D.: JRA-55 based surface dataset for driving ocean–sea-ice models (JRA55-do), *Ocean Model.*, 130, 79–139, <https://doi.org/10.1016/j.ocemod.2018.07.002>, 2018.
- Völker, C. and Köhler, P.: Responses of ocean circulation and carbon cycle to changes in the position of the Southern Hemisphere westerlies at Last Glacial Maximum, *Paleoceanography*, 28, 726–739, <https://doi.org/10.1002/2013PA002556>, 2013.
- Wanninkhof, R.: Relationship between gas exchange and wind speed over the ocean, *J. Geophys. Res.*, 97, 7373–7381, 1992.
- Waugh, D. W. and Haine, T. W. N.: How Rapidly Do the Southern Subtropical Oceans Respond to Wind Stress Changes?, *J. Geophys. Res.-Ocean.*, 125, e2020JC016236, <https://doi.org/10.1029/2020JC016236>, 2020.
- Waugh, D. W., Banerjee, A., Fyfe, J. C., and Polvani, L. M.: Contrasting Recent Trends in Southern Hemisphere Westerlies Across Different Ocean Basins, *Geophys. Res. Lett.*, 47, e2020GL088890, <https://doi.org/10.1029/2020GL088890>, 2020.
- Ziehn, T., Chamberlain, M. A., Law, R. M., Lenton, A., Bodman, R. W., Dix, M., Stevens, L., Wang, Y.-P., and Srbinovsky, J.: The Australian Earth System Model: ACCESS-ESM1.5, *J. South. Hemis. Earth Syst. Sci.*, 70, 193–214, <https://doi.org/10.1071/ES19035>, 2020.